

Physics on a Branched Knotted Spacetime Manifold

Clifford Ellgen* and Garrett Biehle

Pacific Theoretical Physics and Mathematics Research, Pasadena, CA, USA

August 23, 2021

Abstract

This paper reproduces the dynamics of quantum mechanics with a four-dimensional spacetime manifold that is branched and embedded in a six-dimensional Minkowski space [1–4]. Elementary fermions are represented by knots in the manifold, and these knots have the properties of the familiar particles [5–7]. We derive a continuous model that approximates the behavior of the manifold’s discrete branches [8]. The model produces dynamics on the manifold that corresponds to the gravitational, strong, and electroweak interactions [9].

Keywords: quantum mechanics; field theories; special relativity; general relativity; gravitation; knot theory

*cellgen@alumni.caltech.edu

Contents

1	Introduction	3
2	First principles	3
3	Assumptions	7
4	Calculation in Principle	7
5	Lagrangian	8
6	Elementary fermions as knots	11
7	Quantum mechanics	21
8	Interactions	29
9	Conclusion	33
	Appendix A Wave Function Collapse	34
	Appendix B Entropy of Scalar Curvature is $S = -wR$	34
	Appendix C Ricci Flatness of $\mathbb{R}^3 \#(S^1 \times P^2)$	36
	Appendix D Obstruction to Single $\mathbb{R}^3 \#(S^1 \times P^2)$ Annihilation	40
	Appendix E Quark Charge	40
	Appendix F Obstruction to Charged and Unlinked P-contraction	41
	Appendix G Generation Limits	41
	Appendix H Particle Size	42
	Appendix I The Lagrangian is Optimized by a Single Rotation Direction in the Co-dimension	43

1 Introduction

Physics possesses two fundamental theories, general relativity and the Standard Model, both strongly tested and verified in their respective domains [10, 11]. A naive combination of these theories results in unresolvable infinities [12]. Theorists have produced quantum theories of gravity with varying degrees of success. String theory (or M-theory) makes few assumptions and has few parameters, and it produces a quantum theory of gravity along with producing familiar particles [13]. Unfortunately, string theory does not specify a particular choice for the way the vacuum's small dimensions should curl up, and most or all predictions depend on this configuration of the Calabi-Yau space [14]. Loop quantum gravity makes few assumptions and has few parameters, and it produces a quantum theory of gravity and explains a few astrophysical phenomena. Unfortunately, its predictions and explanatory power are quite limited [15].

Like string theory, the theory presented here makes few assumptions and has few free parameters, and it also produces a quantum theory of gravity, as well as the familiar forces and particles. By contrast, however, it has greater explanatory power and the power to predict observations at energies achievable with current technology.

The theory is fully geometric. We assume that the spacetime manifold can be knotted. From knot theory we know that a piecewise linear n -manifold can be knotted only if it is embedded in an $n+2$ -dimensional space [16]. Therefore we assume the 4-dimensional spacetime manifold is embedded in a 6-dimensional Minkowski space. We assume that the manifold is branched so that paths along the manifold may separate and recombine. In this way we introduce interference and thus a probabilistic theory [8].

In this paper we will present the assumptions and structure of this theory, as well as work out the implications of those assumptions in some natural limits and show how the theory works in doing some calculations.

2 First principles

2.1 Dynamical Variables

The dynamical variables are the shape of the 4-dimensional spacetime manifold M ; the vector field A^ν ; and the scalar field ρ , a conformal weight. The vector A^ν is a function of M and is 6-dimensional, and ρ is a function of M . The manifold M is embedded in a Minkowski 6-space Ω . The vector field A^ν exists not only in the tangent space of M but in the tangent space of Ω .

2.2 Derivatives

The metric on Ω is $\eta_{\mu\nu} = \text{diag}(1, -1, -1, -1, -1, -1)$ with coordinates x^ν , where $\nu = 0, 1, \dots, 5$. The manifold M inherits the coordinates x^ν . The restriction of $\eta_{\mu\nu}$ to M is the metric $\bar{\eta}_{\mu\nu}$. If M is flat and in the span of the first four coordinates, then we can choose $\bar{\eta}_{\mu\nu} = \text{diag}(1, -1, -1, -1, 0, 0)$. Often we think of taking covariant derivatives of tensors on a curved manifold M , which requires parallel translation of tensors so that they are defined within the tangent space of the manifold. Covariant derivatives with respect to the metric on the manifold are still well defined. We can also, however, determine the rate of change of a tensor with respect to distances in the 6-space Ω . Because the tensor is defined with respect to the tangent space of Ω , no parallel translation is required and we can use ordinary partial derivatives with respect to x^ν . If T is a tensor on M , we will define the rate of change of T in a direction perpendicular to the manifold to be zero. Let \bar{v}^μ be the projection of v^μ onto M . In this case we can find $\partial_\mu T$, and the rate of change in the direction of vector v^μ is $v^\mu(\partial_\mu T) = \bar{v}^\mu(\partial_\mu T)$. For example, in terms of ordinary partials, the inherited metric can be written

$$\bar{\eta}_{\mu\nu} = x^\alpha_{,\mu} x_{\alpha,\nu}. \tag{1}$$

Here, x^α are the coordinates on the manifold M , inherited from the coordinates of Ω .

2.3 Branched Manifolds

Branched paths on M allow for interference in calculations and thus for a quantum theory [17]. An embedded branched n -manifold is an embedded n -complex such that each point has a well-defined n -dimensional tangent space. In this theory we use M , a branched 4-manifold embedded in a 6-dimensional Minkowski space. We define B to be a branch of M if B is a closed unbranched 4-manifold without boundary and B is contained in M . In Figure 1(c) we see a branched 1+1 manifold Y . The t coordinate is timelike, and the x and y coordinates are spacelike. The branches B_1 and B_2 making up Y are shown in blue in Figure 1(a) and Figure 1(b). The manifold Y is embedded in a 2+1 Minkowski space. The branches separate on the dashed line segments, and on these segments the tangent spaces of B_1 and B_2 coincide. The black curves represent the paths of knots on Y . In this figure, branch B_1 has infinite extent, as does B_2 . They are separate for only a finite time. Where distinct branches B_i intersect, the tangent spaces of the branches must be consistent; this may pose a problem only where the branches B_1 and B_2 separate. Eventually we will be performing sums over multiple histories, and each branch will represent a history.

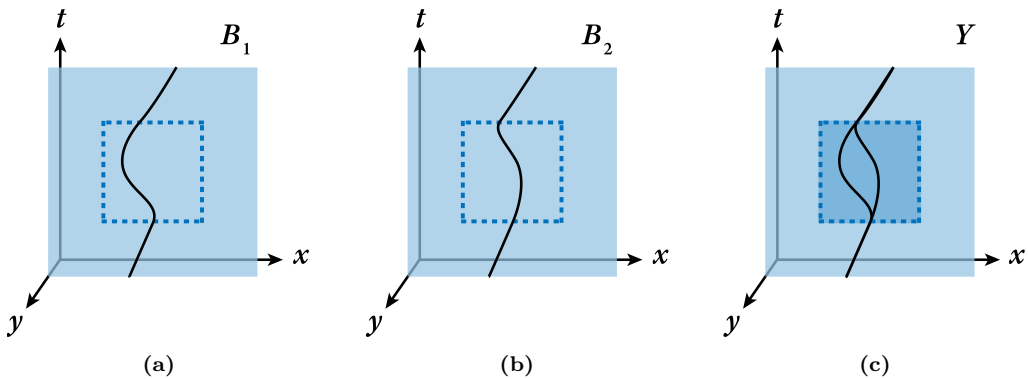


Figure 1: The first two diagrams (a) and (b) show two branches of a 1+1 manifold Y , shown in (c). Y consists of branches B_1 and B_2 , and Y is embedded in a 2+1 Minkowski space. The branches separate on the dashed line. On the dashed line, the tangent space of B_1 is the same as that of B_2 . The black curves are the paths of knots on Y .

2.4 Constraints

So far we have not introduced any constraints on the manifold M or A^ν or ρ . First we introduce a metric $g_{\mu\nu}$ that is distinct from $\bar{\eta}_{\mu\nu}$. We will use the vector field A^ν and the conformal weight ρ to define the metric [18]

$$g_{\mu\nu} = \rho^2 A_{\alpha,\mu} A^\alpha_{,\nu}. \quad (2)$$

In any local neighborhood, we can think of A^ν as being analogous to a coordinate system and the metric $g_{\mu\nu}$ as a measurement of the rate at which A^ν changes, weighted by ρ . The picture of A^ν as a coordinate system will be a helpful metaphor. We constrain A^ν by the equation

$$\det(A_{\alpha,\mu} A^\alpha_{,\nu}) = -1. \quad (3)$$

The tensor $A_{\alpha,\mu} A^\alpha_{,\nu}$ has six dimensions and rank 2. As a matrix in six dimensions, it has determinant zero, but considered as a tensor on the 4-dimensional tangent space of M , the determinant is non-zero, and that is the determinant we use here. For example, $A^\nu = x^\nu$ always satisfies the condition regardless of manifold geometry because $\det(x_{\alpha,\mu} x^\alpha_{,\nu}) = \det(\bar{\eta}_{\mu\nu}) = -1$.

We can determine the Riemann and the Ricci tensors for M relative to $g_{\mu\nu}$. Now we require that the Ricci tensor be flat. We write $\hat{R}^{\mu\nu}$ to indicate Ricci curvature relative to the metric $g_{\mu\nu}$ (in contrast to Ricci curvature relative to $\bar{\eta}_{\mu\nu}$ which we write $R^{\mu\nu}$). Then the constraining equation of the manifold is

$$\hat{R}^{\mu\nu} = 0. \quad (4)$$

We define a branch weight as follows

$$w = (-\det(g))^{1/2} = \rho^4. \quad (5)$$

Ricci flatness implies that the translation of an infinitesimal ball along initially parallel geodesics will preserve the volume of the ball [19]. Therefore the weight w of the ball is preserved by translation along geodesics of $g_{\mu\nu}$. The manifold M is branched, and we assume that the weight is also preserved at branchings. This implies the conformal weight ρ changes at branchings such that the weight w is additive. Ricci flatness $\hat{R}^{\mu\nu} = 0$ therefore extends in a natural way to the branched manifold M . We introduce the assumption that the manifold can branch only a finite number of times by introducing the constraint

$$w \geq 1. \quad (6)$$

A branch with initial weight w can therefore branch no more than w times. In Figure 2 we see branched manifold Y , as well as a spacelike slice through that manifold.

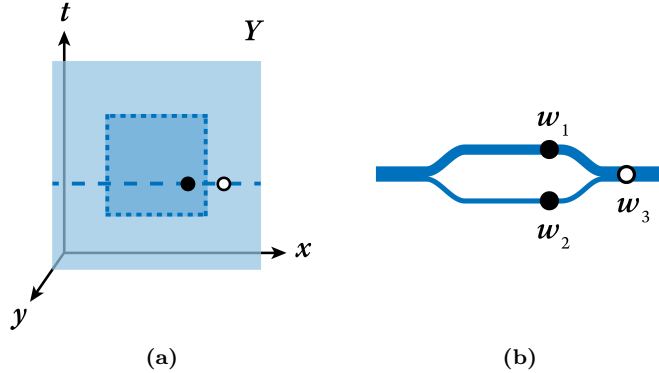


Figure 2: (a) We take a slice through a branched manifold Y . (b) We show that slice. At the branch separation, the branches have weights w_1 and w_2 (black dots). The weights are additive such that the combined branch has weight $w_3 = w_1 + w_2$ (white dot). The thickness of the slice represents the weight but does not correspond to an actual thickness.

As we discussed, Ricci flatness, $\hat{R}^{\mu\nu} = 0$, implies that the translation of an infinitesimal ball along initially parallel geodesics preserves the ball's volume with respect to $g_{\mu\nu}$. If a section of the manifold were to increase in volume over time, we can conserve the integrated weight over the volume by decreasing the weight over the volume. We see this in Figure 3 where the manifold stretches and the weight w compensates for the stretching.

The branch weight w is conserved at branching, and therefore branching reduces the weight on each branch. We see this in Figure 4 where a branched 1+1-manifold stretches. As the volume increases, the weight w decreases to compensate for it. The weight is constrained by $w \geq 1$. As w approaches 1, the only way to continue to extend the volume is by removing weight from the branches and then by reducing the number of branches. When there is only one branch and $w = 1$, it is no longer possible to increase the volume. Thus the constraint $\hat{R}^{\mu\nu} = 0$ implies an exchange between branching and volume.

We have introduced the metric $g_{\mu\nu} = \rho^2 A_{\alpha,\mu} A^\alpha_{,\nu}$ constrained by $\det(A_{\alpha,\mu} A^\alpha_{,\nu}) = -1$, $\hat{R}^{\mu\nu} = 0$, and $w = (-\det(g))^{1/2} = \rho^4 \geq 1$. We will introduce another constraint as follows: Let η^+ be the set of points at positive distance from p and in the future of p relative to $\eta_{\mu\nu}$, as shown in the Figure 5(a). Let g^+ be the set of points at positive distance from p and in the future of p relative to $g_{\mu\nu}$, as shown in Figure 5(b). We require that the sets η^+ and g^+ intersect, as shown in Figure 5(c). The effect of this constraint is to set a limit on $A^\nu_{,\mu}$.

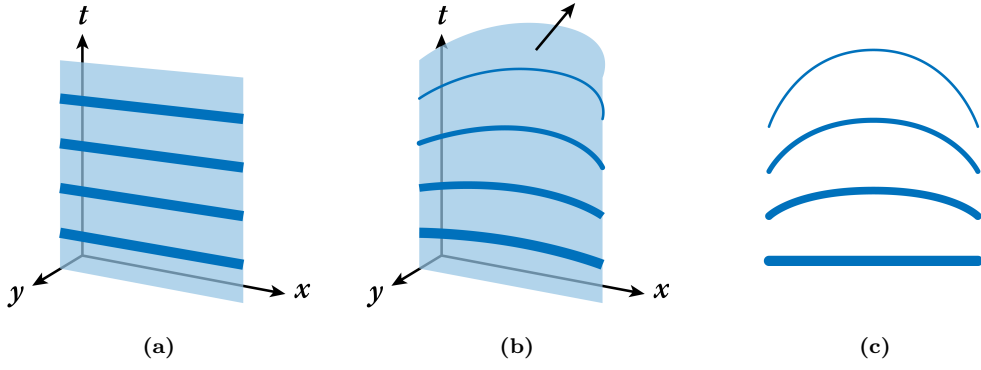


Figure 3: (a) We see a flat 1+1 manifold in which the thickness of the horizontal blue lines represents the weight w in a sequence of spacelike slices. (b) The manifold stretches over time in the direction of the y -axis. The weight w reduces to compensate for the increased volume. (c) We see the sequence of slices from diagram (b). The total weight in each slice is conserved while the volume increases.

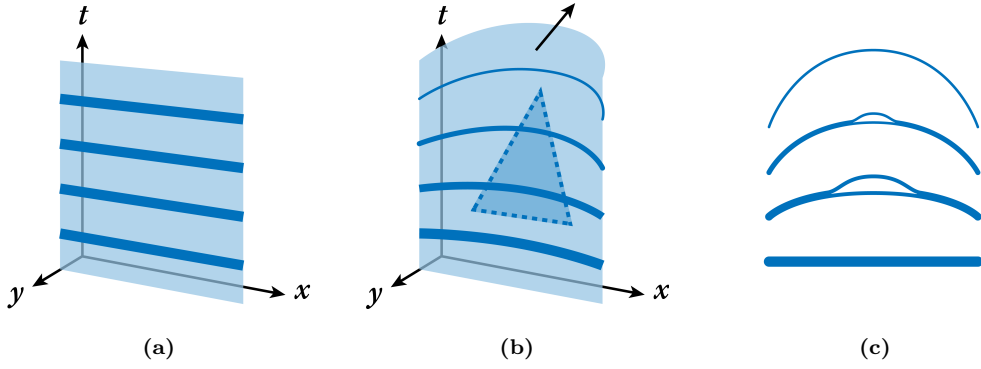


Figure 4: (a) We see a flat 1+1 manifold. (b) The manifold is branched such that the branches separate on the dashed line. The manifold stretches over time in the direction of the y -axis. The weight w reduces to compensate for the increased volume until there can only be one branch. (c) We see the sequence of slices from diagram (b) showing both weight and branching. The total weight in each slice is conserved while the volume increases.

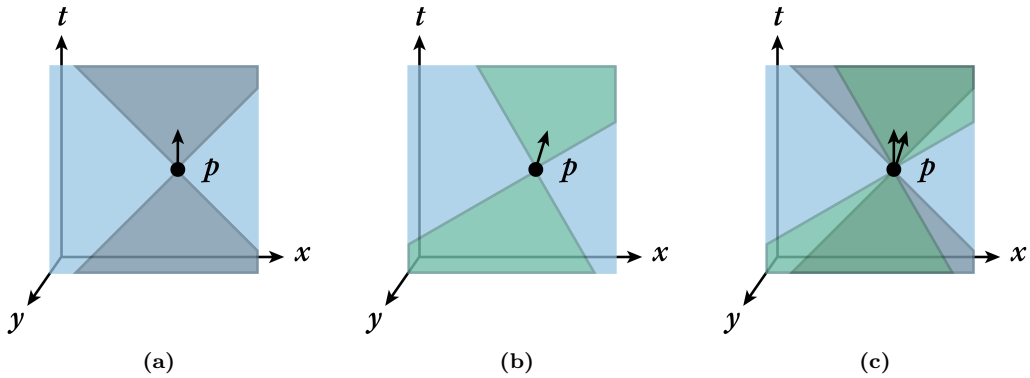


Figure 5: We examine causal cones in a small region such that the geometry and A^ν field are approximately linear. (a) Points in gray have x_ν displacement $\Delta x_\nu \Delta x^\nu \geq 0$. (b) Points in green have A_ν displacement $\Delta A_\nu \Delta A^\nu \geq 0$. (c) The constraint requires that the future A^ν cone intersects the future x^ν cone.

3 Assumptions

The assumptions are the following:

- **We assume a Minkowski 6-space Ω .** The metric on Ω is $\eta_{\mu\nu} = \text{diag}(1, -1, -1, -1, -1, -1)$. The coordinates are x^ν . The dimension of the Minkowski space is chosen to allow the spacetime manifold to form knots.
- **We assume a branched 4-manifold M embedded in Ω .** A *branch* of M is any closed unbranched 4-manifold B without boundary that is contained in M . The manifold is branched so that it can produce quantum properties. The metric $\bar{\eta}_{\mu\nu}$ on M is inherited from Ω . For convenience of coordinates we assume that, if M is flat, then M is in the subspace spanned by x^0, x^1, x^2, x^3 .
- **We assume non-self-intersection of each branch of M .** For any branch B , the branch B cannot intersect itself. This is necessary to prevent knots from spontaneously untying.
- **We assume a vector field A^ν .** The field satisfies $\det(A_{\alpha,\mu}A^\alpha{}_{,\nu}) = -1$.
- **We assume a conformal weight ρ .** Then we define the metric $g_{\mu\nu} = \rho^2 A_{\alpha,\mu}A^\alpha{}_{,\nu}$ and a Ricci curvature $\hat{R}^{\mu\nu}$ based on $g_{\mu\nu}$.
- **We assume a constraint on $g_{\mu\nu}$ relative to $\eta_{\mu\nu}$.** The metrics $g_{\mu\nu}$ and $\eta_{\mu\nu}$ define sets g^+ and η^+ , and we assume that g^+ must intersect η^+ . We recall that, for a point p , the sets g^+ and η^+ are the sets of points at positive distance from p , with respect to the metrics g and η . (In the Minkowski space, the set η^+ is the future light cone of the Minkowski metric η .) This constraint on the metrics produces an important constraint on the electromagnetic potential.
- **We assume Ricci flatness $\hat{R}^{\mu\nu} = 0$ for $g_{\mu\nu}$.** This assumption, and the next two assumptions, prevent multiple kinds of divergent behavior. For example, they prevent the manifold from branching an infinite number of times.
- **We assume that the weight $w = (-\det(g))^{1/2} = \rho^4$ is conserved at branching.**
- **We assume a lower limit $w \geq 1$.**

4 Calculation in Principle

A physical theory must produce predictions for the results of experiments or at least, as in the case of a quantum theory, the probabilities of certain outcomes. In this section we present an overview of calculating the probability that an electron, starting at p at time t_1 will be measured at q at time t_2 , as in a two-slit experiment. The formalism for calculating other probabilities, such as for an electron-positron pair to form a muon and antimuon, involves the addition of other factors.

Calculations in this theory resemble Feynman's sum over histories, except that Feynman's paths cover a continuum of spacetime, and paths in this theory are discrete. For the electron mentioned before, we represent it as a knot in the spacetime manifold M . The manifold M is dynamical, branching and recombining continually. Although there are some constraints on the structure of the manifold, it is underconstrained. Of all the configurations the manifold might take, it tends to take one of maximum entropy [20].

The manifold branches, and knots on the manifold separate along with the branches (as we saw in Figure 1). The knots on the various branches are free to rotate and grow or shrink in the x^4 and x^5 coordinates. We express the magnitude of the knot in the x^4 and x^5 coordinates by ξ and the phase angle of the knot by θ . We describe the knot geometry [21] by the amplitude $a = \xi e^{i\theta}$. When branches recombine, knots on the branches recombine, and the amplitude of the resulting knot depends on the incoming branches and knots. The dynamics of manifold branching and knot recombination determine the paths that yield a desired event or interaction. For example, we could determine the amplitude for an electron starting at p at time t_1 to be measured in a region dV around q at time t_2 . The number of amplitudes in the sum is quite large but not infinite.

We can alternatively approximate the amplitudes on a collection of branches by a complex amplitude ψ , which we will call the quantum amplitude. When collections of branches combine, the quantum amplitude is additive, so that $\psi_{sum} = \psi_1 + \psi_2$. We can calculate the probability using the quantum amplitude, summing over all paths that produce the event or interaction. Later (Section 7) we will show how this approximation reproduces the path integral of quantum mechanics [22].

The primary difference between this theory and standard quantum mechanics is that this theory involves a discrete and finite sum, while quantum mechanics involves a sum over a continuum. We can clarify this statistical description of the branched manifold by introducing an analogy with heat transfer in a crystalline solid. We can model the solid as atoms that transfer momentum during collisions. Carried out in detail, such a calculation is intractable, requiring knowledge of initial conditions that is never available. Nevertheless this model closely resembles the physics. We can also model the solid with a continuous approximation, that is, using the heat equation. This model is not as physical, but it is tractable. In this paper we will show that the dynamics of the discrete, interacting branches, which we claim reflects the physics, can be approximated in a continuous expression, the Feynman path integral. Because we are modeling a system with a finite number of branches, our calculations do not yield the usual infinities [23].

5 Lagrangian

Instead of following the physics tradition of simply stating an expression for a Lagrangian, we will seek to derive a Lagrangian by considering what condition will maximize the entropy of M .

5.1 Branch Cohesion

The probability of an event is proportional to the number of branches that result in that event. Recombination increases the number of branches. In Figure 6(a), two branches result in the event, the left branch and the right branch. In Figure 6(b), four branches result in the event: left-left, left-right, right-left, and right-right. In Figure 6(c), many branches result in the particular event. Recombination increases as branches become closer, so that probability increases as branches become closer. Branches must have the same topology in order to recombine. Therefore, branch recombination can occur only if the knots on the branches match when the branches recombine. As we can see from Figure 6, as the number of recombinations increases, the entropy also increases.

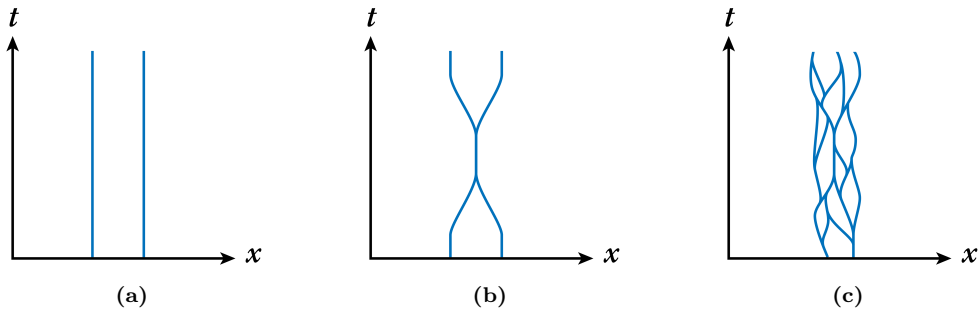


Figure 6: These are three diagrams of a branched 0+1 manifold. (a) We see two branches. (b) We see four branches: left-left, left-right, right-left, and right-right. (c) Staying close increases the number of branches and therefore increases the probability. The manifold maximizes entropy by keeping the branches close.

5.2 Modeling M with an Unbranched Manifold

Because the branches of M stay close to each other, it is possible to approximate the shape of M with an unbranched manifold. We will define Φ_M as the unbranched manifold with A^ν field such that M is as close as possible to Φ_M in both geometry and A^ν field. Let the weight w on Φ_M be the sum of the weights on the branches of M . In Figure 7 we see a model of such an approximation in that the thick light blue band represents a 0+1 branched manifold C . The dark blue curve represents the manifold Φ_C .

We define the Lagrangian \mathcal{L} on Φ_M to be the maximum entropy that M can achieve when it is close to Φ_M . The branched manifold M maximizes entropy, and we can find Φ_M to maximize the entropy and thus the Lagrangian. Once we derive the Lagrangian \mathcal{L} , we will be able to characterize the behavior of M by finding the unbranched manifold Φ_M that maximizes \mathcal{L} [24].

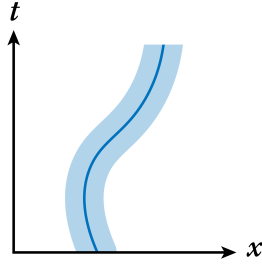


Figure 7: The light blue line represents the branches of a branched 0+1-manifold C . The dark blue line is the manifold Φ_C such that C is as close as possible to Φ_C . The weight w on Φ_C is equal to the sum of the weights on the branches of C .

5.3 Entropy and Curvature

We begin by considering a 1-dimensional manifold C with a fixed length and a fixed boundary. If the manifold is stretched tight, then its entropy is very low, as we see in Figure 8(a). Here the blue curve represents the manifold C . The entropy of C is maximized when C is as close as possible to the straight line connecting its boundary points, as we see in Figure 8(c). If C is a manifold of fixed n -volume with fixed boundary, then the entropy of C is maximized when C is as close as possible to the manifold Φ_C of minimal volume with the same boundary. In order for the manifold Φ_C to have minimal volume, it is necessary that the quantity $\int_{\Phi_C} R d\Phi_C$ be minimized or that the action $S[\Phi_C] = \int_{\Phi_C} -R d\Phi_C$ be maximized, where R is the scalar curvature.

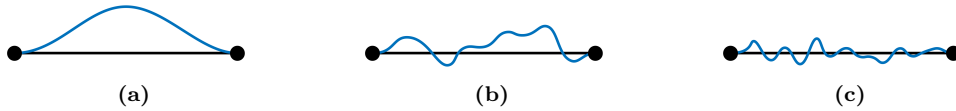


Figure 8: A curve C has fixed endpoints and fixed length. The entropy of C is maximized when C is as close as possible to the straight line connecting its endpoints.

Now we consider a branched 1-manifold C that has a fixed total weight $\int_C w dC$ and a fixed boundary. Again, if the manifold is stretched tight then its entropy is very low. Because the entropy increases with an increasing number of branches, the manifold maximizes its entropy by being as close as possible to the straight line connecting its boundary points. In Figure 9 we see that the stretched manifold has only one branch, while the unstretched manifold has multiple branches and therefore greater entropy. A n -dimensional branched manifold maximizes its entropy by being as close as possible to the minimal volume manifold with the same boundary. This implies the action $S[\Phi_C] = \int_{\Phi_C} -R d\Phi_C$ is maximized [25].



Figure 9: A branched curve C has fixed endpoints and fixed length. The entropy of C is maximized when C is as close as possible to the straight line connecting its endpoints.

In Section B of the Appendix we show that the amount of recombination is proportional to the number of branches. The number of branches is linear in the weight w . The amount of recombination is therefore linear in w . The entropy is linear in the amount of recombination. Therefore, the entropy is linear in weight w , and the action as a function of geometry is

$$S[\Phi_M] = \int_{\Phi_M} -wR d\Phi_M. \quad (7)$$

5.4 Entropy and Field

The A^ν field on M is constrained as described in Section 2.4. The metric $g_{\mu\nu} = \rho^2 A_{\alpha,\mu} A^\alpha_{,\nu}$ and the metric $\eta_{\mu\nu}$ have future causal cones g^+ and η^+ that must intersect. This constraint on the metric $g_{\mu\nu}$ limits the range of $A^\nu_{,\mu}$. In Figure 10(a), the A^0 coordinate and the t coordinate nearly coincide, and the future causal cones η^+ and g^+ nearly coincide. Curves of constant A^0 are not quite the same as lines of constant t . The large number of variations in A^0 indicates a large entropy. In Figure 10(b), the A^ν field is closer to its limit. In the figure, the variations in A^0 must not have the effect of causing g^+ to no longer intersect η^+ . This limits the magnitude of $A^\nu_{,\mu}$ and reduces the entropy in A^ν . To summarize, the constraint on future and past causal cones sets a constraint on the metric $g_{\mu\nu}$, and this limits the range of $A^\nu_{,\mu}$. Furthermore, as $A^\nu_{,\mu}$ approaches this limit, the entropy decreases.

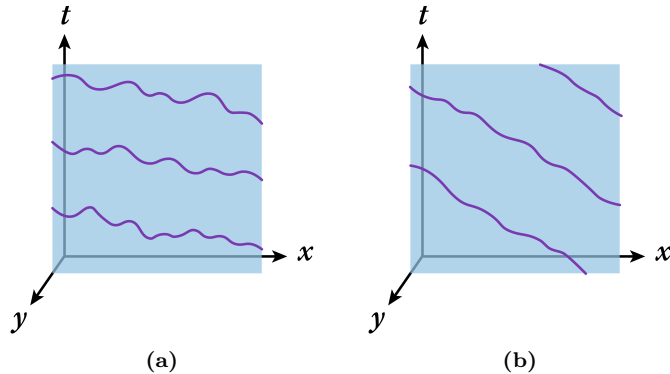


Figure 10: These are two diagrams of sets of constant A^0 . Ricci flatness $\hat{R}^{\mu\nu} = 0$ allows random variation of the field A^ν . The constraint on $g_{\mu\nu}$ relative to $\eta_{\mu\nu}$ limits $A^\nu_{,\mu}$. (a) There is a weak electric field, and $A^\nu_{,\mu}$ is far from its limit. The entropy is large. (b) There is a strong electric field, and $A^\nu_{,\mu}$ is close to its limit. The entropy is small.

So far we have introduced A^ν as a fundamental dynamical variable and connected it to the metric $g_{\mu\nu}$. The field A^ν plays another role in this theory, and it is no coincidence we called it A^ν ; it is the 6-dimensional analog to the electromagnetic potential. Thus we can write an analogous 6-dimensional electromagnetic field tensor on M :

$$F^{\mu\nu} = A^{\nu,\mu} - A^{\mu,\nu}. \quad (8)$$

We want to derive entropy as a function of $F^{\mu\nu}$. In order to do this we need to translate the constraint that the future cone g^+ must intersect the future cone η^+ into a condition on $F^{\mu\nu}$. We begin by considering a weak field limit for A^ν so that $F^{\mu\nu}$ is small.

By eigenvector decomposition, $A^\nu_{,\mu}$ can be described as scaling of vectors and rotations. Only rotations can reduce the intersection of g^+ and η^+ or even cause them not to intersect. Therefore, to leading order, only rotations affect entropy. Note in Figure 5 that a greater rotation leads to a smaller intersection of g^+ and η^+ and in Figure 10 that this leads to less entropy. In general a matrix Q can be decomposed into symmetric and antisymmetric components, $Q = S + A$, where $S = (1/2)(Q + Q^T)$ and $A = (1/2)(Q - Q^T)$. In the case of an infinitesimal rotation matrix, we have $Q \approx I + A$ for infinitesimal antisymmetric A .

Since we define $F^{\mu\nu} = A^{\nu,\mu} - A^{\mu,\nu}$ in analogy with electromagnetic theory, and it is an antisymmetric tensor, it is the rotational component of $A^\nu_{,\mu}$. The Lorentz invariant magnitude of the rotational component of $A^\nu_{,\mu}$ is $F^{\mu\nu} F_{\mu\nu}$.

As the electric field becomes large, either $A^0_{,\nu}$ or $A^\nu_{,0}$ becomes large, and the future causal cone g^+ is rotated relative to the future causal cone η^+ . Entropy decreases. Thus we expect that entropy is proportional to $F^{\mu\nu} F_{\mu\nu}$. The quantity $F^{\mu\nu} F_{\mu\nu}$ decreases on every branch, so we expect entropy to be proportional to the number of branches or, rather, to the branch weight w . We therefore write the linearized Lagrangian as the entropy $\mathcal{L} = w(1/2)F^{\mu\nu} F_{\mu\nu}$ and the action as

$$S[\Phi_M] = \int_{\Phi_M} \frac{1}{2} w F^{\mu\nu} F_{\mu\nu} d\Phi_M. \quad (9)$$

According to Equation (9), the quantity $S[\Phi_M]$ does not diverge no matter how large $F^{\mu\nu}$ is. We know, however, that as the future causal cone g^+ begins to lose its intersection with η^+ , the entropy, the Lagrangian, and the action $S[\Phi_M]$ must diverge. Hence the relationship between the Lagrangian (and action) and $F^{\mu\nu}F_{\mu\nu}$ must be nonlinear. Equation (9) represents the lowest order approximation of the actual (nonlinear) expression.

5.5 Lagrangian and Energy

Including the effects of both the geometry and the A^ν field, we write the Lagrangian on Φ_M as

$$\mathcal{L} = w\left(\frac{1}{2}F^{\mu\nu}F_{\mu\nu} - R\right) \quad (10)$$

and the corresponding action as

$$S[\Phi_M] = \int_{\Phi_M} w\left(\frac{1}{2}F^{\mu\nu}F_{\mu\nu} - R\right) d\Phi_M. \quad (11)$$

Here we have combined eqns. (7) and (9). The first term is $F^{\mu\nu}F_{\mu\nu}$, familiar from electromagnetism. The second term is scalar curvature R , familiar from general relativity. We will see later how these terms generate the properties of electromagnetism and gravity with which we are familiar.

We can use Equation (11) to obtain the energy-momentum tensor. We defined the manifold Φ_M as the unbranched manifold such that M is as close as possible to Φ_M , where M maximizes entropy. The manifold Φ_M does not necessarily coincide with flat space, but we may want to express the measure $d\Phi_M$ in terms of the flat space measure $dt dV$.

If an element of $d\Phi_M$ moves with a velocity β relative to flat spacetime, then we write

$$d\Phi_M = \frac{1}{\gamma} dt dV. \quad (12)$$

We denote the energy-momentum of some matter-energy at rest as $T_{\text{rest}}^{\mu\nu} d\Phi_M$. We can boost to another frame in order to find the energy-momentum $T^{\mu\nu} d\Phi_M$. We can see this illustrated in Figure 11. In Figure 11(a), we see a manifold at rest, while in Figure 11(b) we see a manifold in motion. If some matter-energy has energy-momentum $T_{\text{rest}}^{\mu\nu}$ in the manifold in Figure 11(a), it will have energy-momentum $T^{\mu\nu}$ in the manifold in Figure 11(b), where $T^{\mu\nu}$ is the Lorentz transformation of $T_{\text{rest}}^{\mu\nu}$. If the manifold moves in a direction that is not tangent to the manifold, for example, if Φ_M has motion given by $\vec{\beta} = (1, 0, 0, 0, -\beta, 0)$, then we write

$$T^{\mu\nu} d\Phi_M = \begin{bmatrix} \gamma^2 T_{\text{rest}}^{00} & T_{\text{rest}}^{01} & T_{\text{rest}}^{02} & T_{\text{rest}}^{03} & \beta\gamma^2 T_{\text{rest}}^{00} & 0 \\ T_{\text{rest}}^{10} & T_{\text{rest}}^{11} & T_{\text{rest}}^{12} & T_{\text{rest}}^{13} & 0 & 0 \\ T_{\text{rest}}^{20} & T_{\text{rest}}^{21} & T_{\text{rest}}^{22} & T_{\text{rest}}^{23} & 0 & 0 \\ T_{\text{rest}}^{30} & T_{\text{rest}}^{31} & T_{\text{rest}}^{32} & T_{\text{rest}}^{33} & 0 & 0 \\ \beta\gamma^2 T_{\text{rest}}^{00} & 0 & 0 & 0 & \beta^2\gamma^2 T_{\text{rest}}^{00} & 0 \\ 0 & 0 & 0 & 0 & 0 & 0 \end{bmatrix} \left(\frac{1}{\gamma}\right) dt dV. \quad (13)$$

The change of measure from $d\Phi_M$ to $dt dV$ can confuse the quantity $T^{\mu\nu}$ but we can correct that by referring to the action S that is the integral over space and time. For example, to compare the energy, we can use the integral over space and time, $\int E dt = \int \gamma T_{\text{rest}}^{00} dt dV$, and see that, on some small volume dV , we have $E = \gamma T_{\text{rest}}^{00} dV$. For a volume dV of spacetime, the energy is $\gamma T_{\text{rest}}^{00} dV$ and the momentum is $\beta\gamma T_{\text{rest}}^{00} dV$ in the direction of motion. The familiar expression for rest mass, momentum, and total energy results from motion that is not in the direction of the tangent space of Φ_M at dV . Thus, knots have rest mass because the tangent space of the knot is not parallel to flat spacetime. When a knot moves parallel to spacetime, parts of its geometry extend in directions x_4 and x_5 , and its motion is not in the direction of the tangent space on those parts [26]. See Figure 12.

6 Elementary fermions as knots

Elementary fermions all have the same topology, $\mathbb{R}^3 \# (S^1 \times P^2)$, which we will refer to as a knot and which we will describe in this section. This topology is significant because the equation $\hat{R}^{\mu\nu} = 0$ strongly

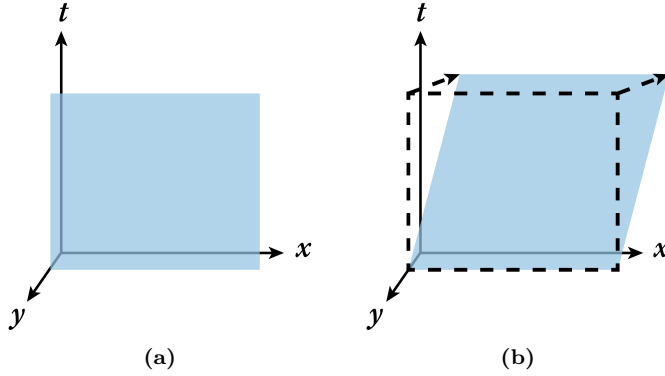


Figure 11: (a) A section of the manifold is at rest. (b) We show a section of the manifold in motion in the $-y$ direction. The energy-momentum tensor $T^{\mu\nu}$ is the Lorentz transformation of $T_{\text{rest}}^{\mu\nu}$, the energy-momentum in the rest frame.

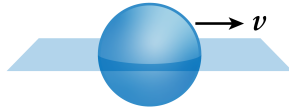


Figure 12: A knot in the manifold is not flat. If the knot is in motion with velocity v then there are points on the knot where that velocity is not in the tangent space. This implies that Lorentz transformations of the energy-momentum tensor at those points correspond to rest mass.

constrains the way that the spacetime manifold M can change topology. The manifold M can, however, change topology to produce pairs of $\mathbb{R}^3 \# (S^1 \times P^2)$. We first describe the knot $\mathbb{R}^3 \# (S^1 \times P^2)$ and then show how to create pairs of $\mathbb{R}^3 \# (S^1 \times P^2)$ subject to $\hat{R}^{\mu\nu} = 0$. Subsequently we show how $\mathbb{R}^3 \# (S^1 \times P^2)$ has properties corresponding to the elementary fermions [27–30].

6.1 Fermion Topological Properties

To describe the topology of an elementary fermion $\mathbb{R}^3 \# (S^1 \times P^2)$, we begin by considering a simpler case in two dimensions, $\mathbb{R}^2 \# P^2$. To make $\mathbb{R}^2 \# P^2$ we begin with $\mathbb{R}^2 - D^2$, the plane with a disk removed. Then we identify the points on the boundary of the disk such that each point is identified with the point that is diametrically opposite. We see this illustrated in Figure 13. The resulting topology is $\mathbb{R}^2 \# P^2$, and it is non-orientable. If we follow a path that passes through the P^2 then we find that the orientation of a coordinate frame translated along that path is reversed. Likewise, if we cut a narrow strip around that path, the result is a Möbius strip.

To make $\mathbb{R}^3 \# (S^1 \times P^2)$ we perform a similar procedure. In cylindrical coordinates, we remove a solid torus T centered around the circle at $z = 0$ and $r = a$. In every constant ϕ slice we have a removed disk, as in the case of $\mathbb{R}^2 \# P^2$. In each slice we perform the same point identification of diametrically opposite points. The result is $\mathbb{R}^3 \# (S^1 \times P^2)$. We see this illustrated in Figure 14.

We note that $\mathbb{R}^3 \# (S^1 \times P^2)$ is also non-orientable. This implies that there is no consistent coordinate frame on the manifold that is based on the rotation group $SO(3)$. However, as with all non-orientable manifolds, we can use a coordinate frame that is based on the double cover of the rotation group. Instead of using the Lorentz transformations $SO(3)$ we use the group $SU(2)$, as we do for elementary fermions.

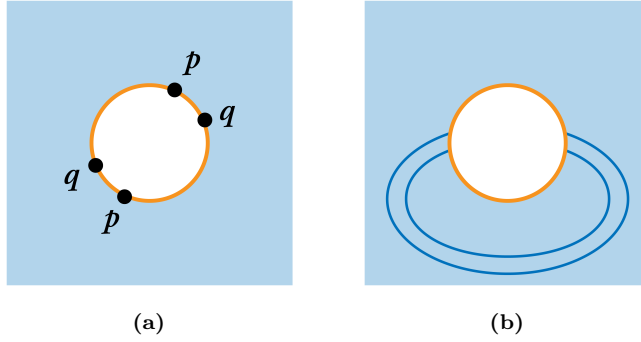


Figure 13: (a) We show $\mathbb{R}^2 - D^2$. The orange circle is the boundary of the removed D^2 . We identify each point on the boundary with the point that is diametrically opposite, for example the points p and q shown here. This makes $\mathbb{R}^2 \# P^2$. (b) We show $\mathbb{R}^2 \# P^2$ with a particular path through the P^2 shown in blue. We see that the outer blue circle connects to the inner blue circle across the P^2 . Translating a coordinate frame along that path reverses the orientation. Cutting a strip around that path produces a Möbius strip [31].

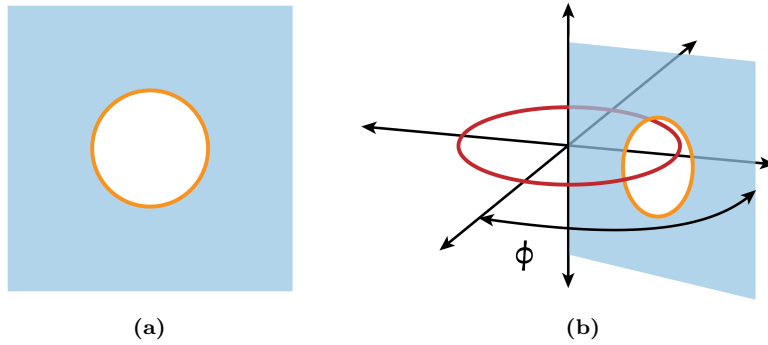


Figure 14: (a) We show $\mathbb{R}^2 \# P^2$. (b) We show a slice through $\mathbb{R}^3 \# (S^1 \times P^2)$ at angle ϕ . In that slice we have $\mathbb{R}^2 \# P^2$.

6.2 Toroidal Coordinates

\mathbb{R}^3 has toroidal coordinates (τ, σ, ϕ) that relate to cylindrical coordinates (r, z, ϕ) as follows:

$$r = a \frac{\sinh \tau}{\cosh \tau - \cos \sigma} \quad (14)$$

$$z = a \frac{\sin \sigma}{\cosh \tau - \cos \sigma}.$$

The sets of constant τ are tori centered around a circle of radius a . At distance zero from the circle we have $\tau = \infty$. At infinite distance from the circle we have $\tau = 0$. The sets of constant σ are spheres such that their intersection with sets of constant τ are orthogonal. Close to the circle, the coordinate σ is a polar angle around the circle. Toroidal coordinates are an orthogonal coordinate system [32–35]. Their properties assist with field equations. We see sets of constant τ and σ illustrated in Figure 15.

6.3 Mapping Coordinates

We use a map from 3 dimensions to 5 dimensions to describe an elementary fermion $\mathbb{R}^3 \# (S^1 \times P^2)$. The coordinates of the 3-space are toroidal coordinates (τ, σ, ϕ) and the coordinates of the 5-space are a mix of toroidal and Cartesian coordinates $(\tau, \sigma, \phi, x^4, x^5)$. If we denote by T the solid torus $\tau > 1$, then we can map from $\mathbb{R}^3 - T$ to \mathbb{R}^5 using

$$X(\tau, \sigma, \phi) = \left(\frac{\tau}{1 - \tau}, \sigma, \phi, \tau \sin(2\sigma), \tau \cos(2\sigma) \right). \quad (15)$$

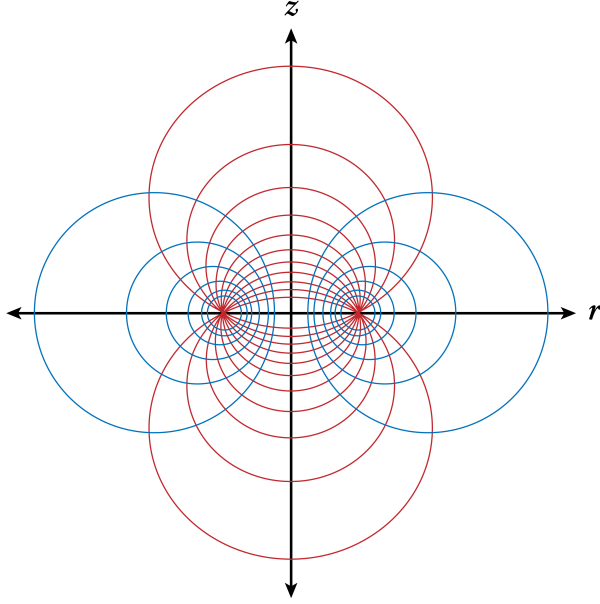


Figure 15: This is a diagram of bipolar coordinates. The diagram shows sets of constant τ in blue and sets of constant σ in red in the rz plane. The value of τ increases to infinity as the size of the blue circles goes to zero. We extend to 3-dimensional toroidal coordinates by including the polar angle ϕ that has the same form as the polar angle of cylindrical coordinates.

The domain of the map is $\mathbb{R}^3 - T$, which is \mathbb{R}^3 with the solid torus T removed, where $\tau > 1$. The map stretches $\mathbb{R}^3 - T$ to cover the missing torus using $\tau \rightarrow \tau/(1 - \tau)$, so that points on the surface of the torus ($\tau = 1$) map to the circle at the center of the torus ($\tau = \infty$). Not only that, the map makes each point on the boundary of T identical to the point that is diametrically opposite it. This happens because we have

$$\begin{aligned}
 X(1, \sigma + \pi, \phi) &= (\infty, \sigma + \pi, \phi, \sin(2\sigma + 2\pi), \cos(2\sigma + 2\pi)) \\
 &= (\infty, \sigma, \phi, \sin(2\sigma + 2\pi), \cos(2\sigma + 2\pi)) \\
 &= (\infty, \sigma, \phi, \sin(2\sigma), \cos(2\sigma)) \\
 &= X(1, \sigma, \phi).
 \end{aligned} \tag{16}$$

(The second equality is due to change of the σ coordinate, which is a polar coordinate such that all values of σ are equivalent at $\tau = \infty$.) We see this illustrated in Figure 16.

The map X produces a knot $\mathbb{R}^3 \# (S^1 \times P^2)$. In addition, however, the condition $\hat{R}^{\mu\nu} = 0$ places a constraint on the conformal weight ρ . See Section C in the Appendix for details.

6.4 Topology Change on M

In this theory we assume that, with respect to $g_{\mu\nu}$, the manifold is Ricci flat, $\hat{R}^{\mu\nu} = 0$. To understand how this relates to particles, knots, and topology change, it helps to compare this assumption to the typical assumption of knot theory [36].

In knot theory it is typically assumed that the manifold must be locally flat. This means that, with respect to the metric $\bar{\eta}_{\mu\nu}$, the Riemann curvature $R^{\alpha\beta\mu\nu}$ of M must be finite. Local flatness prevents the degenerate case that any knot could shrink continuously down to a point, thus disappearing. Likewise, the same process could happen in reverse, thus producing any knot. We see this illustrated in Figure 17. If, however, we do assume that M is locally flat with respect to $\bar{\eta}_{\mu\nu}$, then no topological change is possible [37], and then there could be no particle/anti-particle pair production of knots.

In this theory, we do not assume local flatness with respect to $\bar{\eta}_{\mu\nu}$, but we assume Ricci flatness $\hat{R}^{\mu\nu} = 0$ with respect to $g_{\mu\nu}$. This allows limited topological change, producing knots of the form $\mathbb{R}^3 \# (S^1 \times P^2)$.

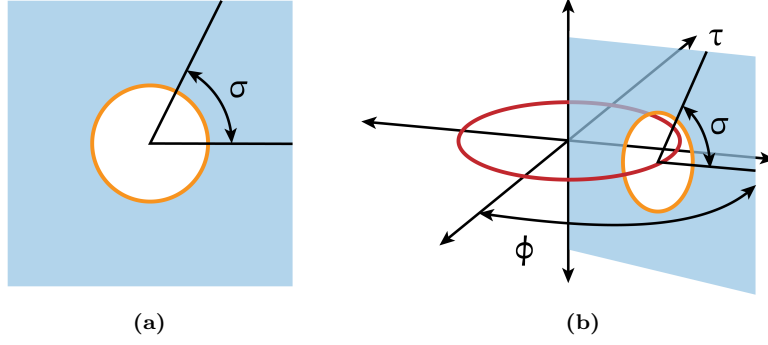


Figure 16: (a) We show $\mathbb{R}^2 - D^2$ with polar angle σ . (b) We show $\mathbb{R}^3 - T$, in toroidal coordinates, with a slice at $\phi = \phi_0$. At the orange circle we have $\tau = 1$. The map X makes opposite points on the circumference of the orange circle identical. This identification of diametrically opposite points creates the topology $\mathbb{R}^2 \# P^2$ in diagram (a) and the topology $\mathbb{R}^3 \# (S^1 \times P^2)$ in diagram (b).

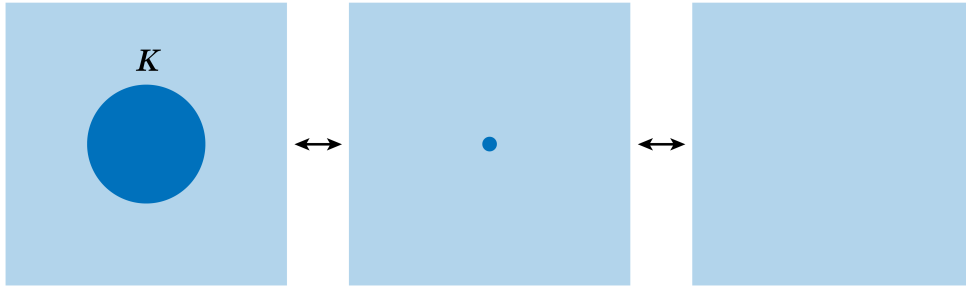


Figure 17: Any knot K , on the left, can be continuously shrunk down to point, thus disappearing. Likewise the same process can happen in reverse, producing any knot from a flat manifold. As the knot shrinks, the Riemann curvature becomes infinite. In knot theory, it is assumed that the Riemann curvature must be finite, which prevents this process. In this theory we assume only that Ricci curvature is zero, $\hat{R}^{\mu\nu} = 0$.

We next show these knots can be created subject to $\hat{R}^{\mu\nu} = 0$.

6.5 Ricci Flat Pair Annihilation and Pair Creation

The dynamics of pair annihilation and creation is an important part of this theory, so we will take a moment to explore the details of this process. We will look at the annihilation of a pair of topologies $\mathbb{R}^3 \# (S^1 \times P^2)$ subject to the condition $\hat{R}^{\mu\nu} = 0$.

In order to see a simple picture of this, consider Figure 18. In the first diagram we see two $\mathbb{R}^2 \# P^2$ topologies coming together. The arrows indicate the direction of $A^0_{,\nu}$ (actually, two components of the electric field). The diagram shows points p and q , each of which is represented in two places in the diagram. In the second diagram the $A^0_{,\nu}$ field is quite strong between the particles. In the third diagram we see points p and q coincide, and the third and fourth diagrams are equivalent. The topology and geometry are then simply \mathbb{R}^2 . In this way we see two $\mathbb{R}^2 \# P^2$ topologies annihilate, much like the annihilation of an electron and a positron [38].

More formally, we can annihilate pairs of $\mathbb{R}^2 \# P^2$ subject to $\hat{R}^{\mu\nu} = 0$. In the above discussion we need points p and q to coincide, as in the third diagram of Figure 18. In the second diagram of Figure 18, p and q are separated by a spacelike vector c^ν . In Figure 19, p and q are separated by a spacelike vector according to the metric $\eta_{\mu\nu}$. We can choose $A^0_{,\nu}$ in order to rotate the light cone at p , so that the light cone for $g_{\mu\nu}$ at p contains q . In this case, $g_{\mu\nu}c^\mu c^\nu = 0$. This corresponds to the third diagram in Figure 18.

This annihilation occurs in one slice of ϕ . We can construct such an annihilation in every slice of ϕ . Thus

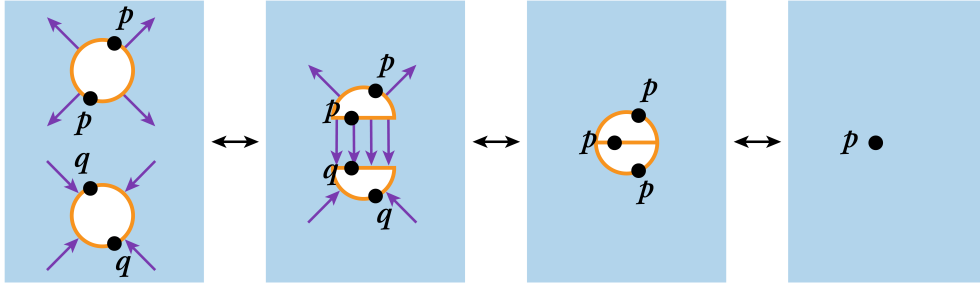


Figure 18: We bring together two P^2 to annihilate. Annihilation requires that the metric $g_{\mu\nu}$ becomes degenerate on the piece of the manifold between the two P^2 . This implies that there is an electric field between the two, indicated by the purple arrows.

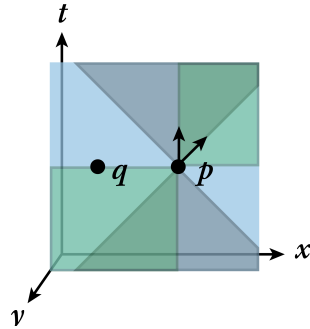


Figure 19: Changing the A^ν field changes the metric $g_{\mu\nu}$. In the diagram there is an electric field and the $g_{\mu\nu}$ distance between the points p and q is zero.

the topology of two particles $\mathbb{R}^3 \# (S^1 \times P^2) \# (S^1 \times P^2)$ can convert to the topology of no particles, which is \mathbb{R}^3 , while maintaining the condition $\hat{R}^{\mu\nu} = 0$ throughout the process. In order to maintain $\hat{R}^{\mu\nu} = 0$, we see that $A^0_{,\nu}$, the electric field, must grow large between the particles before they annihilate.

The process of pair creation is simply the reverse of the annihilation process. During pair creation we see that an $A^0_{,\nu}$ field is created around each knot $\mathbb{R}^3 \# (S^1 \times P^2)$. Each knot subsequently retains this $A^0_{,\nu}$ field as the topologies separate. For the creation of particle/anti-particle pairs this implies opposite charge. See, however Section 6.9 for discussion of charged lepton and neutrino pair creation by a W boson.

6.6 Generations

We have a knot, $\mathbb{R}^3 \# (S^1 \times P^2)$, that corresponds to elementary fermions [39]. We have described that knot using a map from $\mathbb{R}^3 - T$ to \mathbb{R}^5 :

$$X(\tau, \sigma, \phi) = \left(\frac{\tau}{1-\tau}, \sigma, \phi, \tau \sin(2\sigma), \tau \cos(2\sigma) \right). \quad (17)$$

There are other ways of mapping to the knot $\mathbb{R}^3 \# (S^1 \times P^2)$. We can modify the map so that we have

$$X(\tau, \sigma, \phi) = \left(\frac{\tau}{1-\tau}, \sigma, \phi, \tau \sin(2\sigma + n\phi), \tau \cos(2\sigma + n\phi) \right). \quad (18)$$

In each slice of constant ϕ , there is a map of $\mathbb{R}^2 \# P^2$ in \mathbb{R}^4 that has the properties we portrayed in Figure 13. As ϕ varies from 0 to 2π , the map rotates n times in the coordinates x^4 and x^5 . We call such a map $\mathbb{R}^3 \# (S^1 \times P^2)_n$. For every value of $n \geq 0$, the maps of $\mathbb{R}^3 \# (S^1 \times P^2)_n$ are distinct as embeddings. This means that, if $m \neq n$, there is no way to continuously change $\mathbb{R}^3 \# (S^1 \times P^2)_m$ into $\mathbb{R}^3 \# (S^1 \times P^2)_n$ without self-intersection. We propose, for example, that an electron is a charged knot with $n = 0$; a muon, $n = 1$; a tau, $n = 2$.

6.7 Quarks, Linked $\mathbb{R}^3 \# (S^1 \times P^2)$

Two or three of these knots $\mathbb{R}^3 \# (S^1 \times P^2)$ can link [40]. If a knot $\mathbb{R}^3 \# (S^1 \times P^2)$ is linked to another such knot, then it represents a quark. We first describe in outline how such topologies can link to each other, and later we show how these linkings have the properties of quarks [41].

We provide a simple description how two $\mathbb{R}^3 \# (S^1 \times P^2)$ might link by proceeding in stages. Our first goal is to link a pair of P^2 in the 2-dimensional manifold $\mathbb{R}^2 \# P^2 \# P^2$ embedded in 4-dimensional space. First we build a knot $\mathbb{R}^2 \# P^2$ by considering \mathbb{R}^2 in polar coordinates, and we cut out the disk D^2 , which consists of all points such that $r < 1$. Then we map $\mathbb{R}^2 - D^2$ to \mathbb{R}^4 using X_b , such that the coordinate system of \mathbb{R}^4 is polar in the first two coordinates and Cartesian in the last two, (r, θ, x^4, x^5) :

$$X_b(r, \theta) = (g(r), \theta, b \sin(2\theta), b \cos(2\theta)) \quad (19)$$

where

$$g(r) = \begin{cases} 2r - 2 & \text{if } r < 2 \\ r & \text{otherwise.} \end{cases}$$

The function $g(r)$ pulls the boundary of the disk together, because $g(1) = 0$. The points that are diametrically opposite to each other are mapped to the same point in \mathbb{R}^4 . In this way the map $r \rightarrow g(r)$ performs the same purpose as the toroidal coordinates $\tau \rightarrow \tau/(1 - \tau)$ in Equation (15). The x^4 and x^5 coordinates of the map are scaled by the constant b everywhere. The result is $\mathbb{R}^2 \# P^2$. Next, we can use two maps X_1 and X_2 , as in the left figure of Figure 20. The map X_1 is scaled by $b = 1$, and the map X_2 is scaled by $b = 2$. The maps X_1 and X_2 are both maps from $\mathbb{R}^2 - D^2$ to \mathbb{R}^4 . They do not intersect each other but they cannot be separated without intersection. We now truncate X_1 and X_2 to half-planes and join them at the boundary, as in the middle figure of Figure 20. The result is $\mathbb{R}^2 \# P^2 \# P^2$ and the P^2 are linked. If that manifold changes continuously without self-intersection, then the P^2 will remain linked. For example, we can unfold the joined half-planes, as in the right diagram of Figure 20.

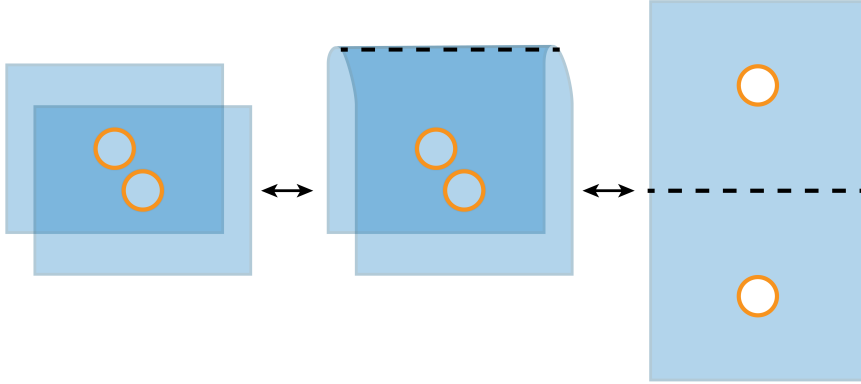


Figure 20: (a) We show 2 copies of $\mathbb{R}^2 \# P^2$. Though the diagram does not indicate it, we assume that they are linked maps X_1 and X_2 . (b) We truncate the maps to half-planes and attach at the boundary (at the top) to make $\mathbb{R}^2 \# P^2 \# P^2$. (c) Then we unfold the $\mathbb{R}^2 \# P^2 \# P^2$. If the unfolding avoids self-intersection then the P^2 remain linked.

Finally, if we fiber the linked pair of P^2 over a circle, that is, rotate the map in the ϕ direction, the result is a linked pair $\mathbb{R}^3 \# (S^1 \times P^2) \# (S^1 \times P^2)$.

We can also link three times: $\mathbb{R}^3 \# (S^1 \times P^2) \# (S^1 \times P^2) \# (S^1 \times P^2)$, as we see in Figure 21.

If we have a pair of topologies represented by the linked pair $\mathbb{R}^3 \# (S^1 \times P^2)_n \# (S^1 \times P^2)_n$ so that the quarks have opposite charge (and same generation n), the pair can annihilate. For a link of three, $\mathbb{R}^3 \# (S^1 \times P^2) \# (S^1 \times P^2) \# (S^1 \times P^2)$, annihilation of any pair is impossible because the annihilation would pass through an intersection with the third quark.

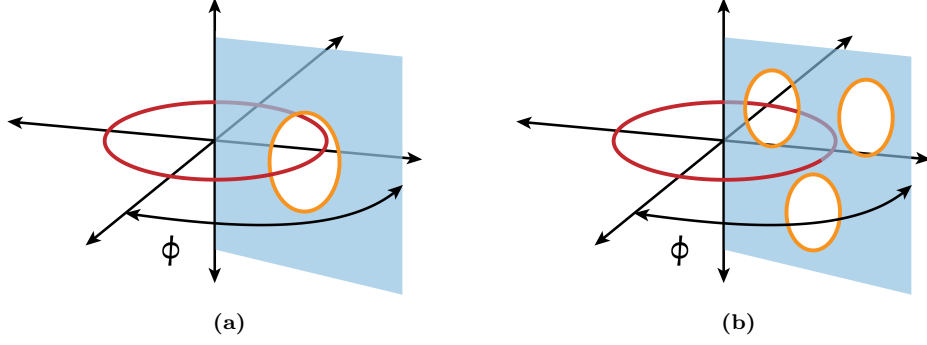


Figure 21: (a) An individual $\mathbb{R}^3 \# (S^1 \times P^2)$ is represented so that the ϕ slice shows a $\mathbb{R}^2 \# P^2$. (b) $\mathbb{R}^3 \# (S^1 \times P^2) \# (S^1 \times P^2) \# (S^1 \times P^2)$ is represented so that the ϕ slice shows a $\mathbb{R}^2 \# P^2 \# P^2 \# P^2$. The diagram does not show the 5-dimensional embedding geometry of the $\mathbb{R}^3 \# (S^1 \times P^2)$ or the 4-dimensional embedding geometry of the ϕ slice. Therefore it is not possible to distinguish from the diagram whether the knots are linked, but if they are linked then they are quarks.

6.8 Charge

We noted at the end of Section 6.5 that, during the creation of fermions, an $A^0_{,\nu}$ field develops, and this field is preserved on one or both of the resulting fermions. If a fermion has a charge, then surrounding the charge we must have a non-zero divergence of the electric field [42]. We see this in Figure 22, which shows the knot $\mathbb{R}^3 \# (S^1 \times P^2)$. Figure 22(a) shows the “top view” of $\mathbb{R}^3 \# (S^1 \times P^2)$. In this diagram the plane is a slice with coordinates x^1 and x^2 as shown. The orange circle represents the torus $X(1, \sigma, \phi)$ (where X is the map associated with $\mathbb{R}^3 \# (S^1 \times P^2)$). The torus has zero volume. A line in Figure 22(a) passes through the knot at two points, seen as vertical orange lines in Figure 22(b).

The second diagram has axes x^0 and x^1 . We plot curves of constant A^0 . We see from Figure 18 that the gradient $A^0_{,\nu}$ comes to a cusp on $X(1, \sigma, \phi)$, and we represent this cusp at the vertical lines in Figure 22. The field cusp has curvature that, by itself, would violate the constraint $\hat{R}^{\mu\nu} = 0$. The geometry of the knot $\mathbb{R}^3 \# (S^1 \times P^2)$ has a corresponding opposite curvature at the cusp that compensates for the field curvature and restores $\hat{R}^{\mu\nu} = 0$. Because of this relation between the field and the particle geometry, the charge is geometrically stuck on the particle unless there is an interaction with another particle [43].

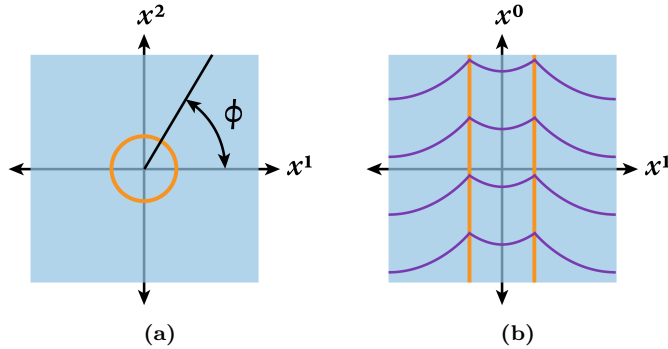


Figure 22: (a) We see a “top view” of a $\mathbb{R}^3 \# (S^1 \times P^2)$ with coordinates x^1 and x^2 as shown. The orange circle represents the torus $X(1, \sigma, \phi)$ where X is the map associated with $\mathbb{R}^3 \# (S^1 \times P^2)$. Relative to the map X , the slice is at an angle of constant σ , and the angle ϕ is shown. (b) We take a slice through $\mathbb{R}^3 \# (S^1 \times P^2)$ at $x^2 = 0$, and we then show that slice in x^0 and x^1 coordinates. The purple curves are sets of constant A^0 . The gradient of those lines is the electric field $A^0_{,\nu}$.

In the case of quarks, the relationship between field curvature and geometric curvature is complicated by the fact that there are multiple $\mathbb{R}^3 \# (S^1 \times P^2)$ whose various curvatures interact with each other. In this paper, we simply assume that quarks have charges of $\pm 1/3$ or $\pm 2/3$ and that particles have integer charge. See Section E in the Appendix for discussion.

6.9 Weak Decay

As we discussed in the previous section, a charged particle has both a field cusp and a corresponding geometric cusp. The constraint $\hat{R}^{\mu\nu} = 0$ implies the field cusp cannot be moved off the knot without also moving the geometric cusp. The geometric cusp can only exist on a knot with the topology $\mathbb{R}^3\#(S^1 \times P^2)$. Therefore, removing the charge from a knot $\mathbb{R}^3\#(S^1 \times P^2)$ requires interaction with another knot of form $\mathbb{R}^3\#(S^1 \times P^2)$. This is a weak interaction.

We describe, for example, the weak decay of a neutron. A down quark with charge $-1/3$ decays to an up quark with charge $+2/3$, and in the process an electron and an electron antineutrino are created. As the down quark becomes an up quark, the charge changes by $+1$, implying a change in the field and geometry. Conservation of charge requires a corresponding change of charge -1 nearby, and this is accomplished by pair creation, specifically, by the creation of an electron and an antineutrino. We saw in Section 6.5 how a pair of $\mathbb{R}^3\#(S^1 \times P^2)$ can be created if there is a strong electric field between them, implying they have different charge. The combination of electric field and geometric curvature that create the pair we call a W boson.

6.10 Generation Change

The topology $\mathbb{R}^3\#(S^1 \times P^2)_n$ is distinct for every $n \geq 0$. Each value of n corresponds to one generation of elementary fermions. For any $m \neq n$ (with $m \geq 0$ and $n \geq 0$) the embeddings $\mathbb{R}^3\#(S^1 \times P^2)_m$ and $\mathbb{R}^3\#(S^1 \times P^2)_n$ are distinct; there is no way to continuously change one into the other without self-intersection. We can, however, construct an embedding that satisfies $\hat{R}^{\mu\nu} = 0$ and makes a transition from m to n , so that the physics will represent a transition from a particle in one generation to a particle another. The transition is represented by the sequence of maps:

$$X_m(\tau, \sigma, \phi) = \left(\frac{\tau}{1-\tau}, \sigma, \phi, \tau \sin(2\sigma + m\phi), \tau \cos(2\sigma + m\phi) \right) \quad (20a)$$

$$X_{m*}(\tau, \sigma, \phi) = \left(\frac{\tau}{1-\tau}, \sigma, \phi, \tau |\sin(\phi/2)| \sin(2\sigma + m\phi), \tau |\sin(\phi/2)| \cos(2\sigma + m\phi) \right) \quad (20b)$$

$$X_{n*}(\tau, \sigma, \phi) = \left(\frac{\tau}{1-\tau}, \sigma, \phi, \tau |\sin(\phi/2)| \sin(2\sigma + n\phi), \tau |\sin(\phi/2)| \cos(2\sigma + n\phi) \right) \quad (20c)$$

$$X_n(\tau, \sigma, \phi) = \left(\frac{\tau}{1-\tau}, \sigma, \phi, \tau \sin(2\sigma + n\phi), \tau \cos(2\sigma + n\phi) \right). \quad (20d)$$

The sequence of maps is shown in Figure 23. We suppress σ ($\sigma = \text{constant}$) and show τ and ϕ , while the thickness of the ring is a representation of the magnitude of displacement in the x^4 and x^5 coordinates. First, we make a continuous transition from the map in Equation (20a) to that in Equation (20b). In the second diagram of the figure, representing Equation (20b), the thickness of the ring goes to zero at $\phi = 0$ because of the scaling factor $|\sin(\phi/2)| = 0$. The geometry can rotate in the σ angle, and the σ rotation on opposite sides of $\phi = 0$ can be independent. This allows the $\mathbb{R}^3\#(S^1 \times P^2)_n$ to untwist or twist around the contraction at $\phi = 0$. We make a continuous transition to the third diagram, representing Equation (20c). Finally, we make a continuous transition from the map in Equation (20c) to that in Equation (20d). In this way, a $\mathbb{R}^3\#(S^1 \times P^2)_m$ can make transition to a $\mathbb{R}^3\#(S^1 \times P^2)_n$.

If there is a slice in which the P^2 contracts to a point, we call this process a P-contraction and call the topology $\mathbb{R}^3\#(S^1 \times P^2)_*$. If the $\mathbb{R}^3\#(S^1 \times P^2)$ is charged and unlinked then it cannot P-contrast. The geometric curvature cannot compensate for field curvature at the P-contraction, and it therefore would not satisfy $\hat{R}^{\mu\nu} = 0$ at the P-contraction. This prevents a spontaneous transition from an muon to an electron, for example. See Sections D and F in the Appendix for details. Uncharged knots $\mathbb{R}^3\#(S^1 \times P^2)$ can P-contrast, and this provides a mechanism by which neutrinos may change from one generation to another.

In the case of a quark, if the knot $\mathbb{R}^3\#(S^1 \times P^2)$ is charged and linked, then it cannot P-contrast for two reasons: the charge is an obstruction at the P-contraction, and the P-contraction itself would pass through intersection with the other quarks. Nevertheless a weak decay of a quark involving a generation change may occur as long as all the linked quarks are involved. For weak interaction involving quark

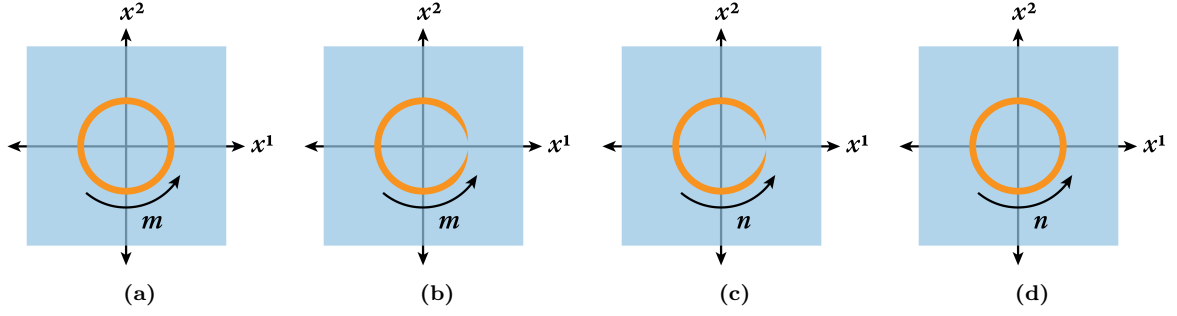


Figure 23: In these diagrams we see the “top view” of a transition from a $\mathbb{R}^3\#(S^1 \times P^2)_m$ to a $\mathbb{R}^3\#(S^1 \times P^2)_n$. Each diagram matches the corresponding map of eqns. (20). The thickness of the orange circle indicates the magnitude of extension into the x^4 and x^5 dimensions. We take a 2-dimensional slice through the $\mathbb{R}^3\#(S^1 \times P^2)$, and the angle ϕ is shown. (a) We see a knot $\mathbb{R}^3\#(S^1 \times P^2)_m$, with the arrow indicating the number of twists with respect to ϕ . (b) We contract the geometry by a factor of $|\sin(\phi/2)|$. At $\phi = 0$ we have $|\sin(\phi/2)| = 0$. This allows the knot to rotate independently around the point of contraction where $\phi = 0$. (c) The knot has rotated around the point of contraction until the number of twists has changed from m to n . (d) We expand the point of contraction back, and there are n twists.

generation change, the quark must pass through an uncharged state by production of particles that conserve charge. Because the product particle’s total charge must be an integer, the quark must change charge by an integer amount. Therefore quark decay converts between up-type and down-type. It also creates a W boson, conserving charge. In the intermediate state where the quark is uncharged, it can convert to an $\mathbb{R}^3\#(S^1 \times P^2)_n$ of different generation n . To avoid intersection with the other quarks, all of the quarks must P-contract in the same ϕ slice so that they are all $\mathbb{R}^3\#(S^1 \times P^2)_*$ and are all P-contracted at the same point. At that point, the fields of the quarks and the W boson add to zero in order to maintain Ricci flatness.

For example, consider the decay of Λ^0 to a proton, an electron, and an electron antineutrino, that is, the decay of a strange quark to an up quark, an electron, and its antineutrino. To change generations, the strange quark must P-contract. To prevent intersection, the other quarks in the Λ^0 must also P-contract at the same location. To maintain the constraint $\hat{R}^{\mu\nu} = 0$ at the P-contraction, there must be some combination of field and geometric curvature that compensates for the field and geometry of the quarks. That combination of field and geometric curvature is a W boson, which results in the production of an electron/antineutrino pair.

6.11 Particle Properties

6.11.1 Neutrinos

An uncharged unlinked knot $\mathbb{R}^3\#(S^1 \times P^2)$ is a neutrino. Since it has no charge, the embedding $\mathbb{R}^3\#(S^1 \times P^2)_m$ may freely change generation m to any n , for $n \geq 0$. Only three generations, however, have been observed. See Section G in the Appendix for discussion.

6.11.2 Charged Leptons

A charged unlinked $\mathbb{R}^3\#(S^1 \times P^2)$ is a charged lepton. Only three generations of charged leptons have been observed. Further exploration of the theory may show that generations with $n > 2$ are not seen because of energy and stability or are disallowed for other reasons.

The charged leptons have the interesting property that they appear pointlike in collisions. In this theory a fermion is a knot of finite size. In Section H in the Appendix we discuss the size of the knot. As a charged lepton approaches another lepton, the radius of the charged lepton decreases. See Section H in the Appendix for details.

6.11.3 Quarks

A charged linked $\mathbb{R}^3 \# (S^1 \times P^2)$ is a quark. It remains to be shown that linked $\mathbb{R}^3 \# (S^1 \times P^2)$ must have charges of $\pm 1/3$ or $\pm 2/3$. Only three generations of quark have been observed. Again, further exploration of the theory may show that generations with $n > 2$ are not seen because of energy and stability or are disallowed for other reasons.

In the previous section we described how interaction of charged leptons with other particles makes them appear pointlike in collisions. By comparison, the size of quarks is influenced by other particles to a lesser degree than charged leptons. Quarks are linked to each other, and their proximity to each other requires relativistic motion and electromagnetic fields to maintain the constraint $\hat{R}^{\mu\nu} = 0$. Interaction with another particle has a relatively smaller effect on quark geometry.

	$(S^1 \times P^2)_0$	$(S^1 \times P^2)_1$	$(S^1 \times P^2)_2$
Uncharged	ν_e	ν_μ	ν_τ
Charged	e	μ	τ
Linked, charged 2/3	u	c	t
Linked, charged 1/3	d	s	b

Table 1: The elementary fermions

7 Quantum mechanics

7.1 Overview of Branch Interaction

The probability that an event occurs is determined by the branches corresponding to that event, and, in turn, this depends on the interaction between manifold branches. This interaction produces the interference that is familiar in quantum mechanics [44–46].

We use the terms “particle” and “knot.” An electron, for example, is a particle. A knot is the topological description of a structure on a branch. In these terms, one real particle is represented by a knot on every branch, and one virtual particle is represented by a knot on some of the branches. This is illustrated in Figure 24.

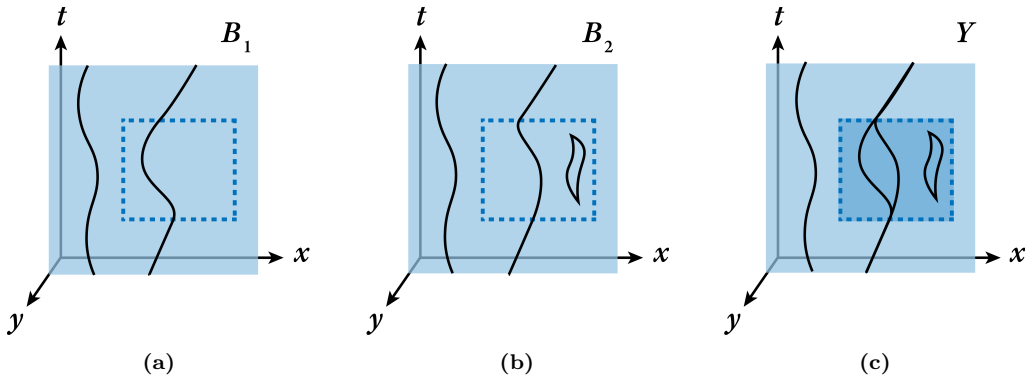


Figure 24: The three diagrams show the branched manifold Y decomposed into constituent branches B_1 and B_2 . The real particles on Y have one knot on both B_1 and B_2 . The virtual particles on Y have one knot on some of the branches (in this case, B_2).

For almost all of this section 7 we will describe the mathematics involved with one real particle. We describe the geometry of the knot with a complex amplitude. When branches recombine, the knots recombine according to a weighted average of their amplitudes. It would be intractable to keep track of all the individual branches and knots in a calculation. Instead we will approximate the particle geometry for all of the branches by developing dynamics on the unbranched manifold Φ_M , introduced in Section 5.2. Then we will show that the branch interactions can be described using a path integral on Φ_M , equivalent

to the path integral of quantum mechanics [22, 47, 48].

When two branches recombine, they must be topologically consistent, so that knots on one branch correspond to knots on the other branch. Furthermore, they must be geometrically consistent. Since the knots on the recombining branches may have different geometries, the recombination forces them to match, leading to particle interference.

In Figure 1, the branched manifold Y has two branches B_1 and B_2 . A single particle is represented by two knots, and the knot on B_1 takes a different path than the knot on B_2 . The geometric characteristics of the knot on B_1 develop differently from those of the knot on B_2 . When the branches recombine, the knots on each of the branches recombine to a knot with geometry that is determined by the geometry of the knots on B_1 and B_2 . To understand how knot geometry is affected by recombination, we begin by describing the geometric characteristics of $\mathbb{R}^3 \# (S^1 \times P^2)$ that correspond to quantum amplitude.

7.2 Particle Geometry and Quantum Amplitude

In Equation (15) we described knot geometry as

$$X(\tau, \sigma, \phi) = \left(\frac{\tau}{1-\tau}, \sigma, \phi, \tau \sin(2\sigma), \tau \cos(2\sigma) \right).$$

We note that the magnitude and orientation (phase angle) of the map relative to the x^4 and x^5 coordinates can be chosen arbitrarily. Thus we may characterize a knot geometry [49] by a single complex amplitude $a = \xi e^{i\theta}$, and write the map $X(a)$ or

$$X(a; \tau, \sigma, \phi) = \left(\frac{\tau}{1-\tau}, \sigma, \phi, \xi \tau \sin(2\sigma + \theta), \xi \tau \cos(2\sigma + \theta) \right). \quad (21)$$

Branch weight $w = (-\det(g))^{1/2}$ also plays a role in quantum amplitude, but we must be careful as to how we include it. First we note that weight is a function of position $w(x)$, and we may denote the weight on branch B_1 as

$$w_1(x) = k_1 w_0(x), \quad (22)$$

where

$$\lim_{x \rightarrow \infty} w_0(x) = 1 \quad (23)$$

and k_1 is the weight coefficient. The standard weight $w_0(x)$ is thus defined at all points on the manifold and depends on the geometry of the knots; it is merely rescaled from the original weight $w(x)$. At any point x the weight coefficient on any branch B_j is given by $k_j = w_j(x)/w_0(x)$. We note that a branch with weight coefficient k could branch k times into branches with standard weight w_0 . In this sense, a branch with weight coefficient k is equivalent to k copies of the same branch. This consideration justifies the name “weight coefficient.”

Suppose two branches B_1 and B_2 , each with a knot, recombine, so that the knots must also recombine. We will assume the knots have maps $X(a_1)$ and $X(a_2)$ with weights $w_1 = k_1 w_0$ and $w_2 = k_2 w_0$. The amplitude a_3 of the recombined branch B_3 is the weighted average of the amplitudes a_1 and a_2 :

$$a_3 = \frac{k_1 a_1 + k_2 a_2}{k_1 + k_2}. \quad (24)$$

The map of the branch is $X(a_3)$. Branch weight is additive at recombination, and therefore the weight coefficient is additive at recombination, so that $k_3 = k_1 + k_2$, or in general

$$k_{\text{sum}} = \sum_j k_j. \quad (25)$$

See the discussion after Equation (5). We see this illustrated in Figure 25. If the branch B_3 splits again into separate branches B_4 and B_5 , then the amplitudes of those branches retain the same weighted average, $(k_4 + k_5)^{-1}(k_4 a_4 + k_5 a_5) = a_3$, and they retain the same total weight coefficient $k_4 + k_5 = k_3$.

Branches maximize entropy by recombining frequently, which implies that branches stay close in order to recombine (see Section 5.1). In order for branches to recombine, the branches must be topologically

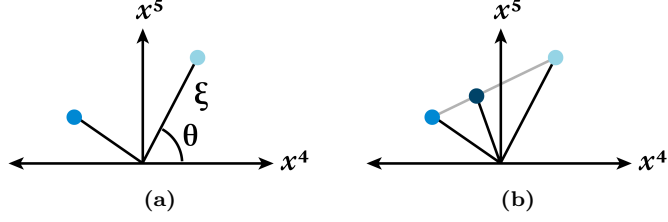


Figure 25: (a) We show two blue dots indicating the amplitudes a_1 and a_2 of two knots, $X(a_1)$ and $X(a_2)$, with weights $w_1 = k_1 w_0$ and $w_2 = k_2 w_0$. (b) If those two knots recombine, they recombine to the weighted average $X(a_3)$ with $a_3 = (k_1 + k_2)^{-1}(k_1 a_1 + k_2 a_2)$, indicated by the dark blue dot.

consistent, and their geometries must be consistent as well. This means that the amplitudes of knots must match before recombining, and this is more likely when the knot amplitudes are similar shortly before recombination. Thus a collection of branches with recombining knots will tend to contain knots of similar amplitudes a_j . On the other hand, we expect knot amplitudes in a collection of branches to diverge from the mean simply because of entropy. Over time we expect the knot amplitudes in the branches to converge to a distribution that maximizes entropy. The weighted average of the knot amplitudes is given by

$$\bar{a} = \frac{\sum_j k_j a_j}{\sum_j k_j}, \quad (26)$$

and this value is preserved during branch recombination [50, 51]. We see this illustrated in Figure 26. Likewise the sum of the weight coefficients $\sum_j k_j$ is preserved during branch recombination.

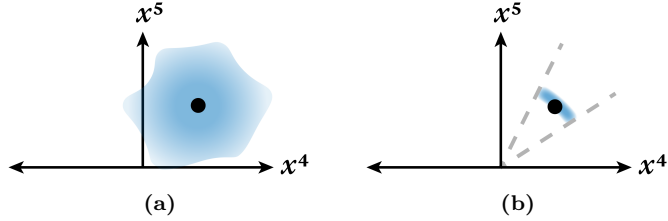


Figure 26: (a) We show a distribution of the amplitudes of many knots. The weighted average $\bar{a} = (\sum_j k_j)^{-1} \sum_j k_j a_j$ is shown by the point. When pairs of knots recombine, they recombine to their weighted averages. (b) After successive recombination and branching, the relative entropic influences determine an equilibrium distribution. The quantum amplitude is $\psi = \sum_j k_j a_j = (\sum_j k_j) \bar{a}$. The total weight $\sum_j k_j$ and the weighted average \bar{a} are preserved during recombination, and therefore the quantum amplitude ψ is well-defined.

In writing a path integral, we will not keep track of all the branches and knots on M individually, but we will model their dynamics using a function on the unbranched manifold Φ_M . We define the quantum amplitude ψ as a complex scalar function on Φ_M . At any point x on Φ_M , we will define B_j as the collection of branches that have a knot near x . We define the quantum amplitude to be

$$\psi(x) = \sum_j k_j a_j. \quad (27)$$

With ψ so defined, we see that we may rewrite ψ as

$$\psi = \left(\sum_j k_j \right) \bar{a} \quad (28)$$

using Equation (26). Where two branches of M recombine, both $\sum_j k_j$ and \bar{a} are preserved by the recombination, and therefore ψ is well-defined at the corresponding location on Φ_M . We distinguish between an amplitude a of a single knot on M and a quantum amplitude ψ of a collection of knots.

We note that the quantum amplitude ψ is additive in the following way: If there are multiple disjoint collections of branches C_m each with its own quantum amplitude ψ_m , then the quantum amplitude of

the union of those collections is the sum of the quantum amplitudes of the collections, so we have

$$\psi = \sum_m \psi_m. \quad (29)$$

The derivation is straightforward. See Section H.1 in the Appendix for details.

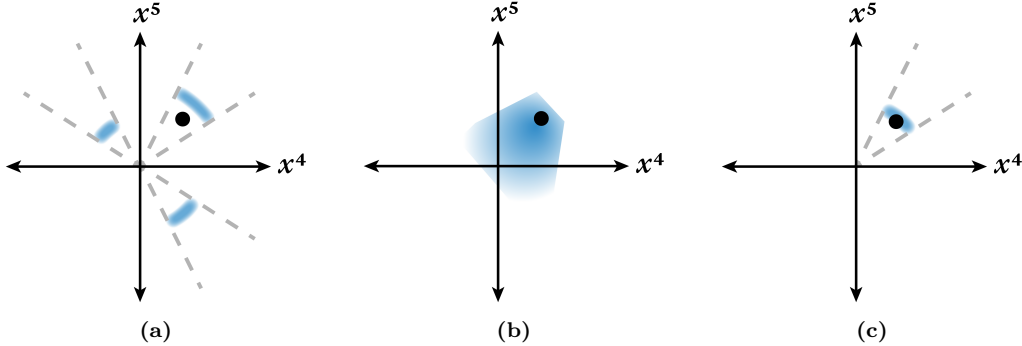


Figure 27: (a) We show the amplitudes of multiple collections C_m of knots. Each collection individually may or may not be in equilibrium. The black point is the weighted average of all the knot amplitudes in all the collections. (b) If those collections C_m begin to recombine they form knots with amplitudes that are weighted averages of knots in C_m . (c) The recombining knots converge to an equilibrium distribution with the same weighted average amplitude. The quantum amplitude in all three diagrams is $\psi = \sum_m \psi_m$.

In Figure 27 we see an illustration of how this recombination occurs. In Figure 27(a) we see the original distribution of amplitudes for the three collections of branches C_m . Pairs of branches from all of the C_m recombine to their weighted average amplitudes, illustrated in Figure 27(b). The distribution of branches converges to a final equilibrium distribution, illustrated in Figure 27(c). Here the weighted average amplitude of the final equilibrium distribution is the weighted average amplitude of the branches of the collections C_m , written $\bar{a} = (\sum_j k_j)^{-1} \sum_j k_j a_j$. Its quantum amplitude is the sum of the amplitudes of the collections, $\psi = \sum_m \psi_m$.

7.3 Phase

The discussion of knot amplitude has not yet included time x^0 or t . We allow the amplitude a to be a function of t , so that we have $a(t) = \xi(t)e^{i\theta(t)}$, and we have

$$X(a(t); t, \tau, \sigma, \phi) = \left(\frac{\tau}{1-\tau}, \sigma, \phi, \xi(t)\tau \sin(2\sigma + \theta(t)), \xi(t)\tau \cos(2\sigma + \theta(t)) \right). \quad (30)$$

To determine how the knot's phase angle changes with time, we return to the description of dynamics on M . Near a knot, fields reduce the entropy of the manifold relative to the vacuum. If the knot is rotating in x^4 and x^5 , then this rotation introduces a factor $1/\gamma$ into $d\Phi_M$ in the Lagrangian of Equation (11). Knots rotate in the co-dimension with angular frequency ω because this reduces the impact of the fields in reducing the entropy. Thus we have

$$X(t, \tau, \sigma, \phi) = \left(\frac{\tau}{1-\tau}, \sigma, \phi, \tau \sin(2\sigma + \omega t), \tau \cos(2\sigma + \omega t) \right). \quad (31)$$

The angle advances at a rate ω that maximizes entropy. If E is the energy of the particle, we will show here that E is proportional to ω .

As the branches of the manifold M recombine, two effects govern the maximization of entropy. On the one hand, frequent recombination of branches increases entropy, as we saw in Section 5.1. On the other hand, entropy increases as the positions and momenta of the branches fill up phase space. In this case, the cohesion effect of recombination reduces the phase space they take up and reduces the entropy. On the one hand, the branches cohere, on the other, they diffuse.

When making a measurement with a real device, we often register a number of quantum states. In this theory we describe that as including a number of branches, all of which contribute to the result. For example, we could imagine a device that measures a particle's location in phase space. If the measurement device has accuracy σ_x in position and σ_p in momentum, then the best measurement we could hope for has $\sigma_x\sigma_p = \hbar/2$. We hypothesize that this limit is the result of multiple branches contributing to the measurement as a consequence of branch cohesion. We therefore interpret this limit as the amount of cohesion between branches. See Section A in the Appendix for details.

Energy and time have a relationship that is analogous to position and momentum. We cannot, however, write $\sigma_E\sigma_t = \hbar/2$ in the same way as $\sigma_x\sigma_p = \hbar/2$ because t does not correspond to an operator. We can, however, consider an observable A with expectation value $\langle A \rangle$ and standard deviation σ_A . If E is the energy of a system, then we have

$$\sigma_A \left(\left| \frac{d\langle A \rangle}{dt} \right| \right)^{-1} \sigma_E = \frac{\hbar}{2} \quad (32)$$

for a best possible measurement. We consider a number of branches. We will call E the energy of a knot on each branch and call A the phase angle θ of the knot. Then we have $\omega = d\langle\theta\rangle/dt$. The knots have a maximally entropic distribution of energies given by [52]

$$P(E) = \lambda e^{-\lambda E} \quad (33)$$

for some λ determined by the knot topology, field potentials, and other details. We calculate the average energy $\langle E \rangle = \lambda^{-1}$ and standard deviation $\sigma_E = \lambda^{-1}$. Therefore we have $\sigma_E = \langle E \rangle$. Then we have

$$\sigma_\theta \left(\frac{d\langle\theta\rangle}{dt} \right)^{-1} \sigma_E = \frac{\hbar}{2} \quad (34a)$$

$$\sigma_\theta \omega^{-1} \langle E \rangle = \frac{\hbar}{2} \quad (34b)$$

$$\langle E \rangle = \frac{\hbar\omega}{2\sigma_\theta}. \quad (34c)$$

We see that the expected value of energy $\langle E \rangle$ is proportional to the angular frequency ω . If the standard deviation of angle is $\sigma_\theta = 1/2$ then we have the familiar relation $\langle E \rangle = \hbar\omega$, but deriving $\sigma_\theta = 1/2$ from the statistics of branch recombination remains to be shown in a future work. Thus we have derived how the phase angle $\theta(t)$ of the amplitude $a(t) = \xi(t)e^{i\theta(t)}$ changes with time.

7.4 Probability

In this section we calculate the probability associated with particle position using a simplified model of branch recombination. For example, in Figure 28(a) we see a branched manifold with two branches and the paths of a particle on the manifold. We may want to know, for example, the probability of measuring a particle at point q rather than at point r on manifold Φ_M , shown in blue in Figure 28(b). In general, the manifold may have many branches and the particle knots may follow many paths. In that case, to obtain the probability of finding the particle at q we use a number of spacelike slices, each slice containing a large number J of points. Between the J points on one slice and the J points on the next slice there are J^2 discrete paths that a knot may take. This is illustrated in Figure 28(c), which shows Φ_M with the knot paths in black and points of recombination in green.

Figure 28(c) shows such a model in which J is three and the number of spacelike slices is three. Figure 29 shows a particular location at which the paths recombine. If we were to make a measurement of the location of the particle, the probability that we would find the particle at that location is determined by the branches that contain the knot at that location. The probability is proportional to the number of branches with knots coming into the location times the number of branches with knots going out. If each path had just one knot on it, then this would be J^2 ; however, each path may have multiple branches associated with it, each with a knot on that path.

In Figure 29 we show the point of knot recombination. Figure 30(a) shows blue lines representing the branches that have a knot. Those branches recombine at the green rectangle. By the rules of branch recombination, any incoming branch can be paired to an outgoing branch in a valid combination. For

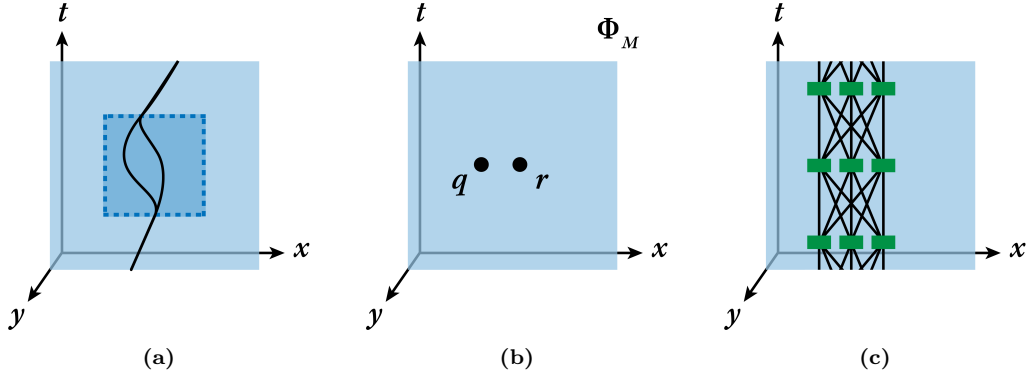


Figure 28: (a) We show a simple branched manifold on which one particle takes two different paths on different branches. We use Φ_M to model the particles of M . (b) The description includes the probability of measuring a particle at particular locations, for example, at points q and r . (c) We restrict the knots to following discrete paths that only recombine at discrete locations then model those paths on Φ_M .

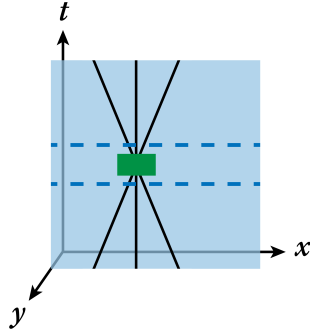


Figure 29: We magnify one of the possible knot recombination locations shown in Figure 28(c). The probability of measuring the knot at that location is determined by the branches that have a knot at that location.

example, Figure 30(b) shows a particular pairing. The number of branches is equal to the number of valid combinations, which is the number of incoming branches times the number of outgoing branches. This format does not have a ready way of expressing the number of branches in all of the incoming paths, and this number is not conserved in recombination. In Section 7.2, however, we defined the weight coefficient of a branch B_j as $k_j = w_j/w_0$. We noted that such a branch could divide into k_j branches of standard weight w_0 . For this reason we can say that the number of branches coming into the location is proportional to the sum of their weight coefficients $\sum_j k_j$. Furthermore, this expression is preserved during recombination and separation, and the total number of branch pairings is proportional to the sum squared. Therefore the probability is $P \propto (\sum_j k_j)^2$.

The probability of measuring a particle at a location is determined not just by the number of branches with the corresponding knot but also by the amount of state space available for the knot at recombination. This is to say that the probability is greater if the amount of “area” in the x^4 and x^5 coordinates occupied by knot amplitudes is larger. (The reason for quotation marks about the word “area” will soon be apparent.) In Figure 31 we see two different equilibrium distributions of knots. Each knot in the equilibrium distribution has a complex amplitude that moves freely within the equilibrium distribution. The size of the equilibrium distribution in state space therefore determines the size of the state space for each of the knots, and the probability is proportional to the size of the state space.

To calculate the size of the state space, we use the standard deviations σ_θ and σ_ξ . In the previous section we assumed that σ_θ is constant. We can calculate σ_ξ here using the time uncertainty relation:

$$\sigma_\xi \left(\frac{d\langle \xi \rangle}{dt} \right)^{-1} \sigma_E = \frac{\hbar}{2}. \quad (35)$$

For an equilibrium distribution, the expectation value $\langle \xi \rangle$ is constant, and we have $d\langle \xi \rangle/dt = 0$. Therefore

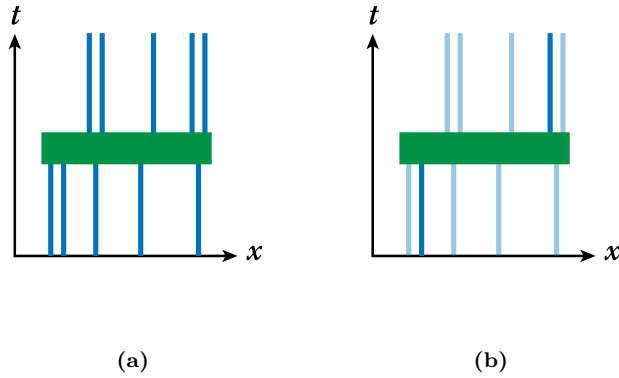


Figure 30: In Figure 29, we depicted a green rectangle where knots recombine, as well as the knot paths that lead into and out of it. **(a)** We show the branches, in blue, that lead into and out of the recombination. The total number of possibilities P includes all choices of branches in and branches out. **(b)** We show an example of one such pair. The number of branches is proportional to $\sum_j k_j$, and therefore $P \propto (\sum_j k_j)^2$.

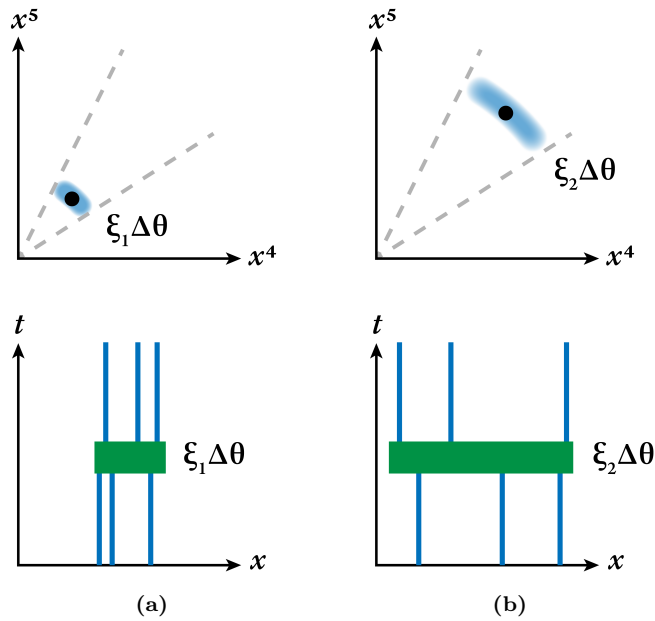


Figure 31: The diagrams show the state space for two different equilibrium distributions of knots. **(a)** The diagrams have $\xi_1 = |\bar{a}_1|$, and **(b)** the diagrams have $\xi_2 = |\bar{a}_2|$. The size of the green rectangle indicates the size of the state space for knot amplitudes of both incoming and outgoing branches. For both incoming and outgoing branches, the size of the state space is proportional to $|\bar{a}|$. Therefore the probability is proportional to the size of the total state space, $P \propto |\bar{a}|^2$.

we have $\sigma_\xi \sigma_E = 0$ and $\sigma_\xi = 0$. The equilibrium distribution converges to having no dispersion of the magnitude $\xi = |a|$ of its knots. The equilibrium distribution of branches in state space is an arc in which the magnitude spread $\Delta\xi$ is infinitesimally small, and the angle spread is $|a|\Delta\theta = \xi\Delta\theta$. In Figure 31 we see the state space for equilibrium distributions with two different magnitudes. In the bottom half of Figure 31 we see a simplified diagram showing the branches coming into the recombination and the branches exiting from it. The width of the green bar indicates the size of the equilibrium distribution (corresponding to $\xi\Delta\theta$). We note that branches coming in to the recombination can have any amplitude within the range of the equilibrium distribution, and branches exiting the recombination can likewise have any amplitude within the range of the equilibrium distribution, with no correlation to the amplitude before recombination. The size of the state space is the range of possibilities for the knot amplitudes, which is the product of the range before recombination times the range after recombination. Therefore the size of the state space is $P \propto (\xi\Delta\theta)^2$. The magnitude of the weighted average amplitude $|\bar{a}|$ is less than the magnitude of the amplitudes that constitute the equilibrium $|a|$, as we see in Figure 32. Since $\Delta\theta$ is constant, we still have $P \propto |\bar{a}|^2$.

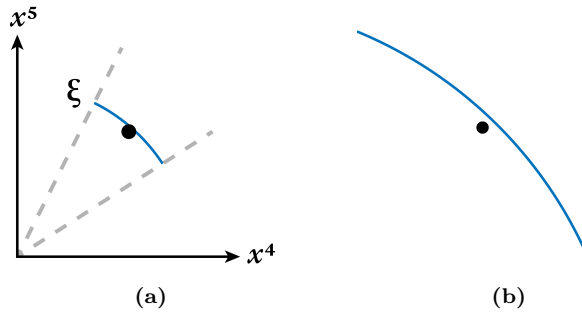


Figure 32: (a) We show an equilibrium distribution with knot magnitudes $\xi = |a|$. Note the infinitesimal spread $\Delta\xi$. (b) We show that the weighted average amplitude \bar{a} has slightly smaller magnitude, $|\bar{a}| < |a|$. Since $\Delta\theta$ is the same for every equilibrium distribution, we still have $|\bar{a}| \propto |a|$.

There are two different contributions to the probability of an event, $P \propto (\sum_j k_j)^2$ and $P \propto |\bar{a}|^2$. Combining the two, we have the familiar relation between probability and quantum amplitude ψ ,

$$\begin{aligned}
 P &\propto (\sum_j k_j)^2 |\bar{a}|^2 = \left| (\sum_j k_j) \bar{a} \right|^2 \\
 P &\propto |\psi|^2.
 \end{aligned}
 \tag{36}$$

7.5 Path Integral

As we mentioned earlier, it would be intractable to keep track of all the individual branches and knots in a calculation. In this section we will demonstrate some steps in deriving an approximation for a transition amplitude between states on M . This approximation involves a path integral on the unbranched manifold Φ_M . Knots on M can interfere only if they can recombine. Knots can recombine only if they have the same topology, and this implies that they represent the same type of particle. Including multiple particles allows for the possibility of pair annihilation, pair creation, and virtual particle pairs. We showed in Section 6.5 that the constraint $\hat{R}^{\mu\nu} = 0$ allows for pair creation and annihilation. The rate of production of virtual particle pairs is determined by entropy maximization. The particles we have described so far have all been elementary fermions, which have topology $\mathbb{R}^3 \# (S^1 \times P^2)$. We will describe the elementary bosons in the next section, Section 8. Every branch can be classified by the interaction of knots on that branch and is represented by a Feynman diagram. In this theory, the transition amplitude is determined by summing amplitudes over all the branches, which is equivalent to summing over histories, or performing a path integral [53, 54].

The manifold M has many interacting branches. Our goal is to make calculations tractable by finding a continuous approximation that describes the interaction of the discrete branches. In Section 7.2 we introduced amplitude $\psi = \sum_j k_j a_j$ for a single particle on Φ_M , a quantity that has the properties of quantum amplitude. In particular, the probability of making a measurement and discovering a particle at a particular location is $|\psi|^2$.

The phase of the knots changes as a function of time and of the knot's path. Let $D(\Delta t)$ be the operator that advances the phase of the knot during time Δt . If q_i is a position, we will call $|q_i\rangle$ an eigenfunction in position space such that $q|q_i\rangle = q_i|q_i\rangle$, where q is the position operator. The amplitude of a transition from q_i to q_j is $\langle q_j|D(\Delta t)|q_i\rangle$. A change of basis yields that the amplitude of a transition from a state $|\phi_i\rangle$ to $|\phi_j\rangle$ is $\langle \phi_j|D(\Delta t)|\phi_i\rangle$. If we consider two states $|\chi\rangle$ and $|\phi\rangle$ separated in time by T , then we can represent the amplitude of a transition by a path integral. We divide the time interval T into N spacelike slices. Then we have

$$\langle \chi|D(T)|\phi\rangle = \langle \chi|D(T/N)...D(T/N)|\phi\rangle. \quad (37)$$

We may insert $1 = \int dq_j|q_j\rangle\langle q_j|$ into this expression, thus allowing the particle to take any path:

$$\langle \chi|D(T)|\phi\rangle = \left(\prod_j \int dq_j \right) \langle \chi|D(T/N)|q_{N-1}\rangle \dots \langle q_1|D(T/N)|\phi\rangle. \quad (38)$$

In Equation (34) we derived $\langle E\rangle \propto \omega$, which we assume to be $\langle E\rangle = \hbar\omega$. With the hint that $\langle E\rangle = \hbar\omega$, we might guess that $H = \hbar d\Theta/dt$, where H is the Hamiltonian and Θ is the operator yielding the phase angle. In this case, the operator that advances the quantum phase is $D(\Delta t) = e^{-iH\Delta t/\hbar}$. We have the equation

$$\langle \chi|e^{-iHT/\hbar}|\phi\rangle = \left(\prod_j \int dq_j \right) \langle \chi|e^{-iHT/(N\hbar)}|q_{N-1}\rangle \dots \langle q_1|e^{-iHT/(N\hbar)}|\phi\rangle \quad (39)$$

where

$$H = \hbar \frac{d\Theta}{dt}. \quad (40)$$

As N goes to infinity, we obtain the path integral for one particle on the right. Some extra formalism is needed to include multiple particles and virtual particles. This produces an expression analogous to the path integral of quantum mechanics.

In Section 7 we have demonstrated how the assumptions of this theory, with its knots and multiple branches, produce the path integral of quantum mechanics as an approximation.

8 Interactions

The dynamics of the branched manifold M results from maximization of entropy [55]. In Section 5 we showed how entropy maximization can be modeled on an unbranched manifold Φ_M with an action $S[\Phi_M] = \int_{\Phi_M} w((1/2)F^{\mu\nu}F_{\mu\nu} - R) d\Phi_M$. We claimed in Section 5.4 that A^ν is the 6-dimensional analog of the electromagnetic potential with electromagnetic field tensor $F^{\mu\nu} = A^{\nu,\mu} - A^{\mu,\nu}$. In this section we will justify this claim. We show how the R term generates the gravitational interaction. Likewise, we will show how particle geometry interacts with the Lagrangian to produce the strong force and electroweak unification.

8.1 Electromagnetism

The Lagrangian has the term $(1/2)wF^{\mu\nu}F_{\mu\nu}$ and higher order terms, although we will consider only the first term. In Section 5.4 we related the maximization of $(1/2)wF^{\mu\nu}F_{\mu\nu}$ to the maximization of the entropy in the A^ν field. The A^ν field has entropy in its random field fluctuations, and those field fluctuations are virtual photons. If the branch weight w is constant, then the term is proportional to $(1/2)F^{\mu\nu}F_{\mu\nu}$. This Lagrangian is the same as that which leads to classical electromagnetism. Electromagnetism is therefore a consequence of maximizing the entropy in virtual photons [56].

Real photons demonstrate interference as well as quantization. Interference is a natural consequence of the Lagrangian term proportional to $(1/2)F^{\mu\nu}F_{\mu\nu}$, but it remains to be shown how field solutions can be quantized. The Lagrangian term is $(1/2)wF^{\mu\nu}F_{\mu\nu}$ with $F^{\mu\nu} = A^{\nu,\mu} - A^{\mu,\nu}$ and $w = (-\det(g))^{-1/2}$, while $g_{\mu\nu} = \rho^2 A_{\alpha,\mu} A^{\alpha,\nu}$ is constrained by $\hat{R}^{\mu\nu} = 0$. We propose that such a nonlinear equation has solutions that are solitons of finite effective width, and these solitons represent real photons [57, 58]. In that case, a plane wave could decompose into photons such that the photons have different locations on

the branches of M . Summing the photons over the branches would re-create the initial plane wave. The measured location of a photon would be a probabilistic result of the interaction of the branches.

Far from knots, a small region of the manifold is approximately flat like \mathbb{R}^4 , and the Lagrangian $(1/2)F^{\mu\nu}F_{\mu\nu}$ is a good approximation of electromagnetism. In that case we will use a coordinate frame such that the two dimensions x^4 and x^5 are perpendicular to M everywhere in the region we are considering. A rotation of the coordinates x^4 and x^5 does not affect the physics in that region. Such a gauge transformation, represented by $SO(2)$ or $U(1)$, leaves the manifold and electromagnetic field unchanged. We are familiar with this gauge group from classical electromagnetism.

8.2 Electroweak

If a knot, representing a fermion, is moving on the manifold M , then near the knot the velocity vector does not lie in the tangent space of the manifold. This is because the knot itself is not flat, like \mathbb{R}^4 . In Figure 12 we see a rough representation of the knot with its velocity in the x^1 direction, and the velocity vector points in a direction that is not in the tangent space. If the knot is charged, then there is energy in the field. In Section 5.5 we saw that a Lorentz transformation perpendicular to the manifold implies expressions for energy and momentum that transform like a four-vector, implying a finite rest mass in the rest frame of the particle. In this case the velocity of the knot has a component perpendicular to the manifold, so the energy in the field is part of the rest energy of the knot.

So a charged particle is the source of field $F^{\mu\nu}$, and, from the analysis above, the transformation of the field yields a part of the rest energy. The scalar curvature term in the Lagrangian (Equation (11)) also contributes to the rest energy. Any fermion is represented by a knot with a particular topology, implying a geometry and a curvature in the manifold. A disturbance of the geometry and curvature of a knot will affect the Higgs field. In particular, if a particle collides with another particle, the geometry around the first particle may vibrate without energy loss. We propose that such a vibration represents a virtual Higgs boson. If the vibration separates from the particle as a transverse wave on spacetime, it will decay to other particles. Such a vibration is a real Higgs boson.

The description of weak decay in Section 6.9 showed that the W boson is a combination of the A^ν field and geometry. The Z boson, by contrast, is a purely geometric effect. Elastic collision of a neutrino with another elementary particle causes a deformation of the particle geometry. The restoring force returns the particle to its initial shape and results in a transfer of momentum. We call that interaction an exchange of a virtual Z boson. We see that the W and Z bosons both have geometry, and therefore they have mass because there are points on the bosons where their tangent space is not parallel to flat space. The geometry of the bosons has finite effective length. Therefore the effective length of the massive boson field is also finite. By contrast, in Section 8.1 we discussed photons, which occur on regions of the manifold that are flat.

In electromagnetism the manifold M is flat (like \mathbb{R}^4), the tangent space is constant, and we derived the gauge group $SO(2) \cong U(1)$, as we saw in Section 8.1. If a particle is present, the knot introduces a certain topology and geometry and also non-constant tangent space, and yet we can find symmetries, or gauge groups, that leave the physics unchanged. To that end we can find some components of the tangent space of M that are unaffected by rotations in x^4 and x^5 , as in our discussion of electromagnetism. These components are represented by the left-pointing arrow in Figure 33. Such a $U(1)$ transformation in x^4 and x^5 leaves the corresponding projection of $F^{\mu\nu}$ unchanged. We can find other components of the tangent space of M that are perpendicular to x^1 , x^2 , and x^3 . These components are represented by the arrow pointing vertically in Figure 33. The projection of $F^{\mu\nu}$ onto the x^4x^5 plane is left unchanged by $SO(3)$ on $x^1x^2x^3$, but the manifold is non-orientable, so we use the appropriate gauge group $SU(2)$. Thus we have the gauge group $U(1) \times SU(2)$.

Far from particles the spacetime manifold is flat, the $F^{\mu\nu}$ field is massless, and the gauge group is $U(1)$. Close to particles the spacetime manifold is not flat, the $F^{\mu\nu}$ field may have mass, and the gauge group is $U(1) \times SU(2)$. This matches the electroweak unification [59–61].

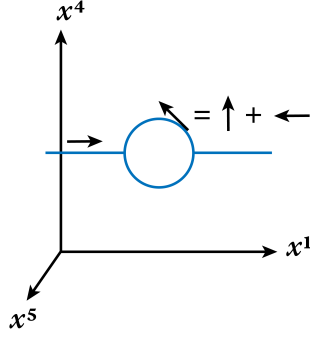


Figure 33: We take a slice through a knot. Vectors tangent to the manifold are represented by arrows. Far from the knot, the tangent vectors are in the span of x^1 , x^2 , and x^3 . Rotation of the coordinates x^4 and x^5 has no effect on the manifold. Close to the knot, the manifold is not flat. We decompose the tangent vectors into components that are perpendicular to flat space and components that are parallel to flat space. The components that are perpendicular to flat space are unaffected by rotation of x^1 , x^2 , and x^3 .

8.3 Strong

Quarks are linked knots $\mathbb{R}^3 \# (S^1 \times P^2)$ (Figure 21). Since a branch of the manifold cannot intersect itself, the quarks are unable to unlink, and this results in quark confinement. When the quarks are sufficiently close to each other, there is no mechanism by which they exert a force on each other, resulting in asymptotic freedom. As the distance between two quarks increases, however, the knot is stretched, and the R term in the Lagrangian produces a geometric interaction that increases the energy. We propose that the geometric interaction is equivalent to the exchange of a gluon.

In order to derive a symmetry group for the strong force and to derive an analogy for the color charge, we will consider three quarks making up a hadron and, in particular, the five spatial coordinates describing the center of those quarks. Thus we will use the notation q_n^j , where $n = 1, 2, \text{ and } 3$ identifies the quark, and $j, 1 \leq j \leq 5$, identifies the index of the 5-vector. We will choose an origin of coordinates to represent the zero-momentum frame, so that $\sum_n q_n^j = 0$. The quarks are linked and cannot be separated. We could create a model in which their position vectors have some maximum magnitude, which we will take to be 1. We could write $|q_n^j| \leq 1$ for each q_n , that is, each quark must be within distance 1 of the center. Alternatively, we could add a (non-physical) sixth coordinate q_n^6 to each position vector and require $|q_n^j| = 1$ for each n . We now perform the map

$$(q_n^1, q_n^2, q_n^3, q_n^4, q_n^5, q_n^6) \rightarrow (q_n^1 + iq_n^2, q_n^3 + iq_n^4, q_n^5 + iq_n^6). \quad (41)$$

The ordinate has complex coefficients, unit length, and zero sum, so that it is analogous to the color charge. The transformation that preserves these properties is $SU(3)$, so we expect $SU(3)$ to be the gauge transformation for three quarks that are near each other. Indeed if three quarks are near each other, they do not exert a force on each other, and any change of coordinates that preserves the properties in the previous paragraph will not affect the physics. Such a coordinate change will result in different complex 3-vectors of unit length and zero sum of coordinates.

It may appear that we have ten degrees of freedom in choosing the coordinates of the quarks, five for each of three quarks, minus five for the constraint $\sum_n q_n^j = 0$. Adding a sixth coordinate adds three degrees of freedom, but the constraint $\sum_n q_n^6 = 0$ removes one, that is, it sets one of the sixth coordinates. We have three additional equations $|q_n^j| = 1$ for $n = 1, 2, \text{ and } 3$. Two such equations constrain the other sixth components, but the last equation must constrain one of the ten degrees of freedom with $1 \leq j \leq 5$. Thus there are nine degrees of freedom when determining the geometry near linked knots. This is in contrast to the 8-dimensional group $SU(3)$. More work needs to be done to show the relationship between knot physics and the strong force, but this section shows how quark confinement, asymptotic freedom, and $SU(3)$ emerge from the elements of knot physics [62–76].

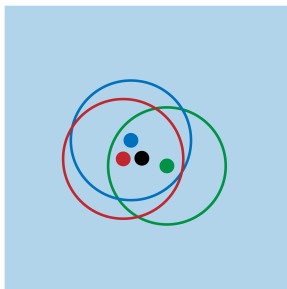


Figure 34: The “top view” of three linked quarks is shown. Each quark is a different color and the center point of each quark is indicated by a smaller circle of the same color. The center of the particle is the black circle. The quark centers are displaced from the particle center by 5-vectors q_n^j , where n labels the quark and j labels the spatial coordinate.

8.4 Gravity

8.4.1 Classical Gravity

In Equation (11) we see that the Lagrangian contains the term $-wR$, which is the same form as the Lagrangian that generates general relativity. Hence we expect this theory to generate general relativity in the classical limit [77, 78].

8.4.2 Geometry

We want to see how this term affects the geometry of the manifold. Matter and energy impose order on the manifold and, in this sense, reduce entropy. If we denote by \mathcal{L}_m the effect of matter and energy on the Lagrangian, we may write the action as

$$S[\Phi_M] = \int_{\Phi_M} w(\mathcal{L}_m - R) d\Phi_M. \quad (42)$$

Here we include all the sources in the term \mathcal{L}_m . If the branch weight w is constant, then we have the Lagrangian of general relativity $\mathcal{L} = \mathcal{L}_m - R$.

To maximize entropy, a macroscopic region with matter and energy moves in the co-dimension. The region rotates in the coordinates x^4 and x^5 , and the rotation reduces its proper time, introducing the factor $1/\gamma$ to $d\Phi_M$. Reducing the proper time reduces the effect of matter and energy on the action $S[\Phi_M]$. In Section 7.3 we derived that a knot will rotate in dimensions x^4 and x^5 . The gravitational rotation is much larger than the quantum scale, so that it is not the rotation of individual branches but rather the collective rotation of all the branches, as in Figure 35. In Figure 35 we see a spacelike 2-dimensional slice of M with a region of matter and energy. The entropy of the region is reduced by an amount \mathcal{L}_m by the introduction of matter. To reduce the effect of the matter and energy on the Lagrangian, the region rotates in x^4 and x^5 . In the diagram we take a slice, indicated by the dashed line. In the diagram on the right, we see that slice of the manifold in the dimensions x^1, x^4 , and x^5 . The slice of the manifold extends into the dimensions x^4 and x^5 , and it is rotating. Its rotation reduces the proper time and therefore reduces the measure $d\Phi_M$. In this way, the manifold maximizes entropy.

8.4.3 Dark Matter

The branch weight w determines the number of branches in a given region. Over small cosmological distances branch density will tend to spread evenly as entropy maximizes. Thus w becomes approximately constant.

The large-scale distribution, on the scale of galaxies, may not be uniform. These variations have a

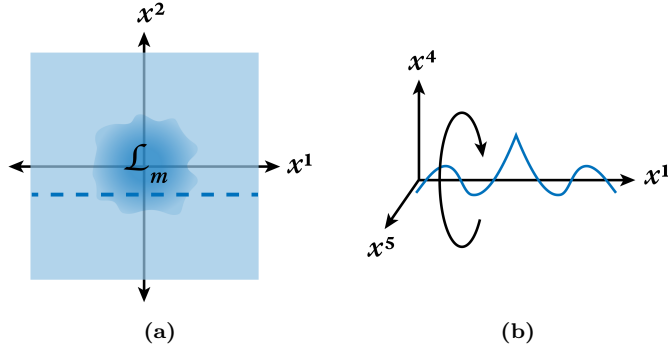


Figure 35: (a) We show a spacelike 2-dimensional slice of M . There is a region with matter and energy. The matter and energy reduce the entropy by an amount \mathcal{L}_m . The dashed line indicates a slice through the region. (b) We show that slice with its extension into x^4 and x^5 . The manifold rotates in the dimensions x^4 and x^5 , and this rotation reduces its proper time.

gravitational effect and are not propagated by a particle. In this way, the branch weight variations appear to produce the properties of dark matter.

8.4.4 Rotation in the Co-dimension

In Figure 35 we see rotation of the spacetime manifold in the co-dimension. The rotation is of the form $(x^0, x^1, x^2, x^3) \mapsto (x^0, x^1, x^2, x^3, b \sin(k_j x^j), b \cos(k_j x^j))$ where $j = 0, 1, 2, 3$, and b is the amplitude. To maximize entropy, the manifold rotates in the same direction everywhere. (For proof, see Section I in the Appendix.)

9 Conclusion

In this paper we have described a theory in which physics takes place on a branched 4-dimensional spacetime manifold M embedded in a 6-dimensional Minkowski space Ω . The manifold M has a conformal weight ρ and a field A^ν , from which we derive the metric $g_{\mu\nu}$. The manifold M is constrained to be Ricci flat with respect to $g_{\mu\nu}$, and it observes several other constraints, but otherwise it randomizes and assumes a shape that maximizes entropy. The assumption of entropy maximization allows us to write a Lagrangian.

We represent fermions by topological knots $\mathbb{R}^3 \# (S^1 \times P^2)$ on the manifold M . Depending on how the knot is embedded in the 6-dimensional space Ω and depending on the properties of A^ν on the knot, the knot may represent various charged or uncharged leptons. Furthermore, if the knot is linked to other knots, then it represents a quark. These knots assume the properties of the familiar particles.

The manifold M branches and recombines continually, and the knots on M branch and recombine as well. This recombination leads to interference effects. Using an approximation of the theory, we have shown that it reproduces the probabilistic results of quantum mechanics.

Near a knot, the geometry produces a gauge group $SU(2) \times U(1)$, exactly like the electroweak gauge group. When we consider the properties of linked knots in a baryon, they produce the gauge group $SU(3)$, just like that for the strong force. The Lagrangian for the theory contains a term that matches that for general relativity, so in a suitable regime the theory reproduces gravitation. These and other clues indicate that in suitable regimes the theory reproduces the properties of the four forces, although more work is needed.

Appendix A Wave Function Collapse

This theory explains what happens when events on a quantum scale are magnified to a macroscopic scale. When elementary quantum mechanics predicts a solution of the superposition of two or more states, the state that is measured is determined by entropy.

Entropy is proportional to the rate of branch recombination. Branches can recombine only when they have matching knots. If branches have knots that do not match, then they cannot recombine. Without recombination the entropy is less. Entropy maximization therefore implies that branches will tend to create states that are similar enough to allow recombination.

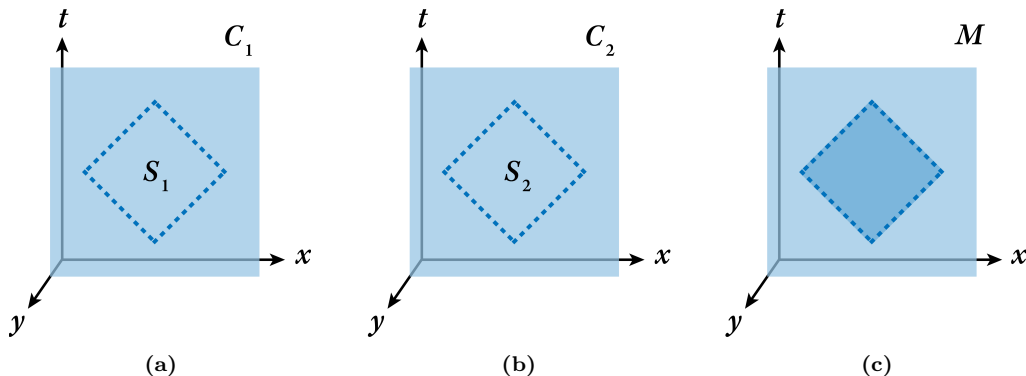


Figure A1: The branched manifold M is shown separated into two collections of branches C_1 and C_2 that are in two different states S_1 and S_2 inside the dotted line. If every intermediate state between S_1 and S_2 has low entropy then this prevents recombination between C_1 and C_2 inside the dotted line. If C_1 and C_2 cannot recombine, then this reduces the entropy from a case in which all the branches are in S_1 or S_2 . Eventually the collections C_1 and C_2 do collapse to one of the states S_1 or S_2 , so that they can resume recombination. In the diagram, C_1 and C_2 are in increasingly divergent states S_1 and S_2 that later collapse to a single state.

Consider the example of a measurement of particle location such that the particle is equally likely to be found in either of two potential wells. The measuring apparatus magnifies the effect of the state to macroscopic level, and it indicates the location of the particle. In Figure A1 we see a depiction of this process. Initially, one collection of branches C_1 have the particle in potential well number 1, state S_1 , and another collection of branches C_2 have the particle in well 2, state S_2 . At the time of measurement, there is an interaction with the particle in the well. The branches of C_1 begin the magnifying process to indicate the particle's location in well 1, state S_1 , and the branches of C_2 begin the process to indicate well 2, state S_2 . Then C_1 and C_2 are in increasingly different states S_1 and S_2 . The branches of C_1 and C_2 cannot recombine where their states are different. This implies a reduction of the entropy of recombination. All of the intermediate states between S_1 and S_2 are at low entropy, and therefore disfavored, but entropy increases as branches from S_1 (or S_2) pass through the intermediate states to S_2 (or S_1). Then C_1 and C_2 collapse to a single state, either S_1 or S_2 . This happens on the quantum scale. By the time the measurement has been magnified to macroscopic size, the state has already collapsed.

Appendix B Entropy of Scalar Curvature is $S = -wR$

The branched manifold M has entropy in its branching. Because of the constraint $\hat{R}^{\mu\nu} = 0$, increasing the volume of the branches of M decreases the number of branches, as in Figure 4 and in the discussion following Equation (6). The total weight w is conserved. The manifold M is centered around the unbranched manifold Φ_M . With fixed boundary, decreasing the volume of Φ_M increases the number of branches of M . In Figure 9 a branched 1-manifold C with fixed endpoints changes geometry to approach the straight line connecting the endpoints. We can say that C is centered around an unbranched manifold Φ_C (not shown in the diagram) and that Φ_C approaches the straight line. The number of possible branches on C is maximized when Φ_C is exactly equal to the straight line.

If the number of states of M is P , then the entropy of M is

$$S = \ln P. \quad (43)$$

The number of states of M is linear in the number of branches, and we see in Figure 6 that the number of branches increases as the amount of recombination increases.

On M there are many branches recombining. To determine the entropy in these recombinations, we determine how the branches are involved in the recombinations. Directly calculating the number of branches of M is intractable (see the third diagram of Figure 6). Instead, we will approximate the number of branches in M by assuming that k branches recombine and separate repeatedly. If we have just k branches recombining with each other over time Δt , then the number of states is $P \propto k^{f\Delta t}$, where f is the frequency of the recombinations. We see this by applying the branch counting technique shown in Figure 6. We see in Figure A2 that the manifold has some total weight w . The total number of branches in M is proportional to w . We can say that there are w/k recombinations happening in parallel.

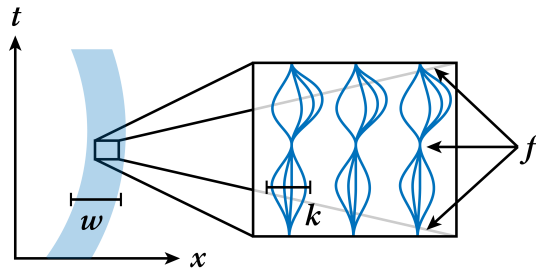


Figure A2: This is a cross-section of the branched manifold M . The total number of branches of M is proportional to the total weight of all the branches of M . This is equal to the weight w on Φ_M (we define w on Φ_M as the sum of the weights w on the branches of M). Looking at a small piece of the cross section we see that there are many branches recombining. Let k be the average number of branches in any particular recombination. Then there are w/k recombinations happening in parallel. Let the frequency of recombinations be f .

We include all the branches of M by including w/k interactions happening in parallel, each interaction containing k branches, all happening with frequency f . Since each interaction has $k^{f\Delta t}$ possibilities, the number of states is

$$P \propto (k^{f\Delta t})^{w/k} = k^{f\Delta t(w/k)}. \quad (44)$$

Then the entropy over time Δt is

$$S\Delta t = \ln P \propto \left(\frac{fw}{k}\right)\Delta t \ln k. \quad (45)$$

The numbers k and f are constant, and therefore we have $S = \ln P \propto w$. The result, that $S \propto w$, does not depend on any choice of k or f , nor does it depend on our model.

If we stretch the branched manifold M , then Φ_M has a corresponding change in volume, $V \rightarrow V'$. The constraint $\hat{R}^{\mu\nu} = 0$ implies Φ_M has a change of weight $w \rightarrow w'$ such that $w'V' = wV$. For a fixed boundary on an infinitesimal ball, a small change in the scalar curvature R increases the volume by $V' \approx V(1 + R)$. Then the weight is affected by $w'V(1 + R) \approx wV$, which implies

$$w' \approx w/(1 + R). \quad (46)$$

Therefore the entropy is related to scalar curvature by $S \approx w/(1 + R)$. Linearizing around $R = 0$ we have $S \approx w - wR$. Considering only the variation in R we have $S \approx -wR$.

Appendix C Ricci Flatness of $\mathbb{R}^3 \# (S^1 \times P^2)$

C.1 Flatness from a Lagrangian

In Section 6 we described a procedure for creating the knot $\mathbb{R}^3 \# (S^1 \times P^2)$, and throughout the paper we have introduced coordinates for the knot on M . In this section we will derive conditions on ρ that will assure Ricci flatness, $\hat{R}^{\mu\nu} = 0$. In following sections, we will elaborate on features of the Ricci flat geometry.

To find a Ricci flat vacuum, we can use the Einstein-Hilbert action

$$S_{EH} = \frac{1}{16\pi} \int_M d^4x \sqrt{-g} R. \quad (47)$$

This equation is familiar from general relativity. In the presence of matter and energy, we modify this action with a corresponding additional term in the Lagrangian. To appropriately modify this action to suit the topology $\mathbb{R}^3 \# (S^1 \times P^2)$, we treat the topological surgery as a manifold boundary ∂M and then include a Gibbons-Hawking-York boundary term S_{GHY} that accounts for that boundary [79–81]:

$$S_{EH} + S_{GHY} = \frac{1}{16\pi} \int_M d^4x \sqrt{-g} R + \frac{1}{8\pi} \int_{\partial M} d^3y \epsilon \sqrt{h} K. \quad (48)$$

In this equation, h_{ab} is the induced metric on the boundary, \sqrt{h} its determinant, K is the extrinsic curvature, ϵ is equal to $+1$ where ∂M is timelike and -1 where ∂M is spacelike, and y^a are the coordinates on the boundary. Varying the action with respect to the metric $g_{\alpha\beta}$, subject to the condition $\delta g_{\alpha\beta}|_{\partial M} = 0$ gives the Einstein equations.

The surgery attaches antipodal points, therefore we constrain the Lagrangian such that the metric g must be equal on opposite sides of the surgical attachment. In terms of the maps, this means that $g(X(1, \sigma, \phi)) = g(X(1, \sigma + \pi, \phi))$. The metric g is equal on both sides of the cross-cap surgery, which implies that the boundary metric h is also equal on both sides. Because the surgery attaches antipodal points to each other, the extrinsic curvature must be opposite on antipodal points,

$$K(X(1, \sigma, \phi)) = -K(X(1, \sigma + \pi, \phi)). \quad (49)$$

In the following sections we show how to use the conformal weight ρ and the embedding of the manifold to achieve this constraint.

C.2 Flatness in Two Dimensions

We begin by finding Ricci flat solutions for $\mathbb{R}^2 \# P^2$, the 2-dimensional case. To make $\mathbb{R}^2 \# P^2$ we remove a disk from a plane and set each point on the disk boundary identical to the point that is diametrically opposite. Although the disk with the plane removed, $\mathbb{R}^2 - D^2$, is flat, when we identify points to create $\mathbb{R}^2 \# P^2$, it is no longer flat unless we meet certain conditions for ρ . We draw a circle on the manifold around the P^2 as in Figure A3(a). We cut along the circle to produce a manifold with boundary, which we call M_2 , as in Figure A3(b). Then we apply the Gauss-Bonnet theorem to M_2 :

$$\int_{M_2} \hat{R} dA + \int_{\partial M_2} k_g ds = 2\pi \chi(M_2). \quad (50)$$

In this equation, the symbols are the conventional ones for this theorem. The geodesic curvature k_g provides a measure of how much a curve deviates from a geodesic in a manifold, and the Euler characteristic χ depends only on the topology of the manifold. We have $\hat{R} = 0$ on M_2 . The Euler characteristic of P^2 is $\chi(P^2) = 1$. The Euler characteristic of M_2 (equivalent to $P^2 - D^2$) is $\chi(M_2) = 0$. The geodesic curvature $k_g = 0$ at every radius. Zero geodesic curvature requires that perpendicular lines passing through the circles do not diverge relative to $g_{\mu\nu}$. We conclude that the red lines in Figure A3(c) span an equal length on each circle. Therefore, on a flat $\mathbb{R}^2 \# P^2$ the circumference is constant at every radius,

as illustrated in Figure A3(c). The manifold has the same geometry as a cylinder. If we consider M_2 as an embedding in the same sense as the mapping

$$X(a; \tau, \sigma, \phi) = \left(\frac{\tau}{1-\tau}, \sigma, \phi, \xi\tau \sin(2\sigma + \theta), \xi\tau \cos(2\sigma + \theta) \right), \quad (51)$$

then we can describe the geometry of M_2 in terms of the magnitude ξ . In the degenerate case that the magnitude ξ goes to zero, M_2 approaches a flat disk, and the weight ρ compensates for the geometry such that $C\rho = b$ for circumference C and constant b . In Figure A3(c) we see a $\mathbb{R}^2 \# P^2$ with a few circles shown as examples of circumferences around the P^2 . Ricci flatness requires that those circles have constant circumference, with conformal weight ρ such that $\rho = b/C$.

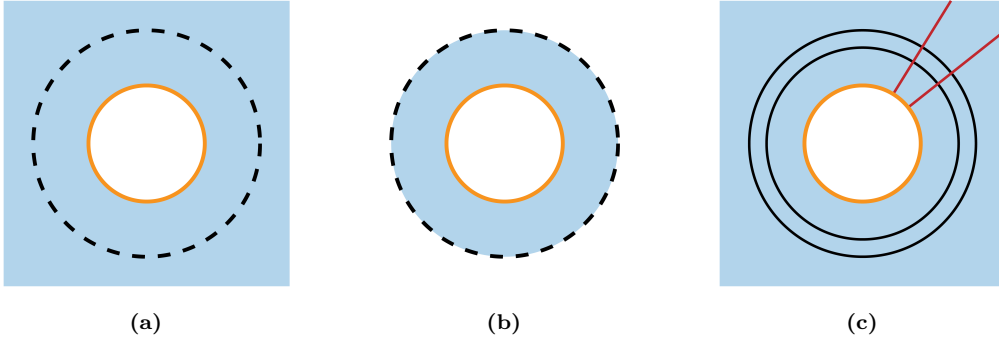


Figure A3: (a) We see a $\mathbb{R}^2 \# P^2$ with a circle drawn around it. (b) We cut on the circle to produce the manifold M_2 . If $\hat{R} = 0$ on the interior of M_2 , then, by the Gauss-Bonnet theorem, the geodesic curvature on the boundary of M_2 is $k_g = 0$. This is true for any circular boundary we draw. (c) For example, we see some examples of circular boundaries on which the geodesic curvature is zero. Zero geodesic curvature requires that perpendicular lines passing through the circles do not diverge relative to $g_{\mu\nu}$. For example, the red lines shown do not diverge. We conclude that the red lines span an equal length on each circle. Therefore any such circle has constant circumference relative to $g_{\mu\nu}$, with conformal weight ρ such that $C\rho = b$.

We now consider a more general solution for Ricci flatness on \mathbb{R}^2 . In two dimensions, for any harmonic function κ , if a metric $\bar{\eta}_{\mu\nu}$ is Ricci flat then the metric $e^{2\kappa}\bar{\eta}_{\mu\nu}$ is also Ricci flat [82]. In our case we start with Ricci flat $\bar{\eta}_{\mu\nu}$, and we construct a harmonic function κ . For multiple source points p_i there is a harmonic function

$$\kappa(x) = \sum_i -\ln(d(p_i, x)) \quad (52)$$

where $d(p_i, x)$ is the distance from p_i to x . Then we set

$$\rho = e^\kappa \quad (53)$$

and

$$g_{\mu\nu} = \rho^2 \bar{\eta}_{\mu\nu} \quad (54)$$

is a Ricci flat metric. If there is only one source, this solution exactly matches the solution we obtained before for the degenerate P^2 , which was $\rho = e^\kappa = 1/d = b/C$. Thus we can replace the points p_i by a degenerate P^2 (one for which its embedding has magnitude $\xi = 0$). If the magnitude ξ increases, then the displacement of the embedding into x^4 and x^5 increases, which increases the length of a path around the P^2 . Therefore, increasing the magnitude ξ increases the circumference C . Ricci flatness requires that the weighted circumference $C\rho$ is constant, and therefore ρ must change to preserve the weighted circumference $C\rho$.

Next let us consider the case of \mathbb{R}^2 with natural metric $\bar{\eta}_{\mu\nu} = \text{diag}(1, 1)$. In this slice let us assume there is a P^2 with $\xi = 0$ at the point $p_1 = (1, 0)$ and at the point $p_2 = (-1, 0)$, as in Figure A4(a). (Later we will use this plane as the slice $\phi = 0, \phi = \pi$ through $\mathbb{R}^3 \# (S^1 \times P^2)$, but we completely suppress the third dimension for the moment.) We begin by finding the harmonic function $\kappa(x) = \sum_i -\ln(d(p_i, x))$ and then setting $\rho = e^\kappa$. Now we use the metric $\rho^2 \bar{\eta}_{\mu\nu}$ with degenerate P^2 at each of the points p_i . In Figure A4(b) we see bipolar coordinates, which are the 2-dimensional version of toroidal coordinates with

ϕ angle suppressed. The circles in blue are the same as the circles of constant τ in toroidal coordinates. Relative to $\rho^2\bar{\eta}_{\mu\nu}$, these circles have constant circumference $C\rho$. We can increase the magnitude ξ of both of the P^2 as desired, compensating for the geometry by reducing ρ as needed. Bipolar coordinates give an isometric mapping between the cylinder $\mathbb{R} \times S^1$ and the Ricci flat $\mathbb{R}^2\#P^2\#P^2$. The blue circles of Figure A4(b) are mapped from the circles of the cylinder corresponding to the S^1 fiber. The red circles of Figure A4(b) are mapped from the parallel lines of the cylinder corresponding to the \mathbb{R} fiber.

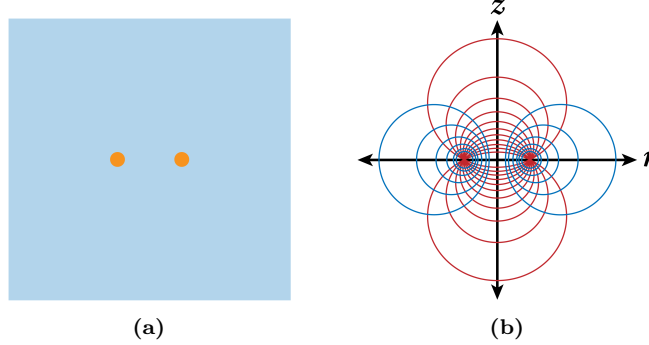


Figure A4: (a) We see a $\mathbb{R}^2\#P^2\#P^2$ with a P^2 at the point $p_1 = (1, 0)$ and at the point $p_2 = (-1, 0)$. We will later use this as a slice through a $\mathbb{R}^3\#(S^1 \times P^2)$. (b) We see bipolar coordinates centered around p_1 and p_2 . Bipolar coordinates are the 2-dimensional version of toroidal coordinates with the ϕ coordinate suppressed. The circles of constant τ , shown in blue, have constant circumference relative to $\rho^2\bar{\eta}_{\mu\nu}$. The circles of constant σ , shown in red, are also geodesics relative to $\rho^2\bar{\eta}_{\mu\nu}$.

C.3 Flatness in 2+1 Dimensions

Now we introduce the time dimension. The usual inherited metric for a flat manifold is $\bar{\eta}_{\mu\nu} = \text{diag}(1, -1, -1)$. Introducing the manifold $\mathbb{R} \times (\mathbb{R}^2\#P^2\#P^2)$, we have P^2 on the manifold at $p_1 = (t, 1, 0)$ and $p_2 = (t, -1, 0)$. We can scale the metric as above to get $\rho^2\bar{\eta}_{\mu\nu}$. Volume in three dimensions, however, scales as ρ^3 , and we find that the time dimension makes the conformal scaling no longer Ricci flat. If we want to write a volume element, then we must compensate for the time dimension, so we use symmetry and motion. Rather than beginning with initial metric $\bar{\eta}_{\mu\nu} = \text{diag}(1, -1, -1)$, we introduce an embedding of the manifold that is in motion with some velocity β in x^4 and x^5 . We set β such that $\gamma = \rho$. If we describe the metric using a coordinate chart, then the inherited metric is $h_{\mu\nu} = \text{diag}(1/\gamma^2, -1, -1) = \text{diag}(1/\rho^2, -1, -1)$. Thus the metric includes the factor $\rho(\Delta t/\gamma) = \Delta t$, and the metric becomes $\rho^2 h_{\mu\nu}$, which is Ricci flat.

In the previous section, we mapped isometrically to the manifold $\mathbb{R}^2\#P^2\#P^2$ from the cylinder $S^1 \times \mathbb{R}$. Here, we can map isometrically to this manifold $\mathbb{R} \times (\mathbb{R}^2\#P^2\#P^2)$ from $\mathbb{R} \times (\mathbb{R} \times S^1)$. The manifold $\mathbb{R} \times (\mathbb{R} \times S^1)$ with its natural metric is Ricci flat. Therefore this manifold with its embedding and conformal weight is also Ricci flat. Again, the magnitude ξ of the P^2 can be expanded, and ρ is reduced to compensate. Now that ρ is linked to motion through $\rho = \gamma$, we see that reducing ρ reduces the velocity.

C.4 Flatness in 3+1 Dimensions

Introducing the third spatial dimension, we again find that adjustments are necessary to produce Ricci flatness. The Weyl metric gives a description of any axially symmetric Ricci flat geometry in terms of two potential functions, U and V . In cylindrical coordinates (t, r, z, ϕ) the Weyl metric is

$$ds^2 = e^{2U} dt^2 - e^{-2U} (r^2 d\phi^2 + e^{2V} (dr^2 + dz^2)). \quad (55)$$

The potential function U satisfies the Laplacian

$$\nabla^2 U = U_{,zz} + U_{,rr} + (1/r)U_{,r} = 0 \quad (56)$$

and the potential function V is related in the following way

$$V_{,r} = r((U_{,r})^2 - (U_{,z})^2) \quad (57a)$$

$$V_{,z} = 2rU_{,r}U_{,z}. \quad (57b)$$

We can extend the description that we used for 2+1 dimensions by saying that the harmonic function κ is analogous to the potential function U . For 3+1 dimensions, we use a harmonic function κ whose source is the degenerate $S^1 \times P^2$. The function κ is uniquely determined by its source, up to a constant factor. The function U , which also satisfies the Laplacian, is proportional to κ . Subsequently we can solve for V in terms of U .

Ideally we would solve for exact solutions U and V . Here, we will sketch a derivation of approximations for U and V . To derive an approximation, we consider a slice of \mathbb{R}^4 with constant t and constant ϕ , and we observe the behavior of U and V near the degenerate $S^1 \times P^2$ at $(r, z, \phi) = (1, 0, 0)$. Furthermore, we consider behavior only along the r coordinate, so that $z = 0$. In this case, we have

$$U = -\ln|r-1| \quad (58a)$$

$$V_{,r} = r(U_{,r})^2 = r\left(\frac{d}{dr}(-\ln|r-1|)\right)^2. \quad (58b)$$

For Equation (58a) we have used Equation (52). In the limit of approaching the degenerate $S^1 \times P^2$, the radial term r is approximately constant in comparison to the derivatives. We therefore have

$$V_{,r} = (U_{,r})^2 = \left(-\frac{d}{dr}\ln|r-1|\right)^2 = \left(\frac{1}{r-1}\right)^2 \quad (59)$$

$$V = -\frac{1}{r-1}. \quad (60)$$

We obtain the same result by performing the integral in Equation (59) exactly and ignoring the smaller term near the $S^1 \times P^2$. Near the $S^1 \times P^2$, the effect of the function V dominates over that of $U = -\ln|r-1|$. Just inside the torus, two nearby points with slightly different r will have a large ds according to Equation (55), since $r \lesssim 1$ and $V \gg 0$. Just outside the torus, two nearby points with slightly different r will have a small ds since $r \gtrsim 1$ and $V \ll 0$. As we go from the inside of the ring to the outside, the sign of V changes, and we see that, in the limit as we approach the degenerate $S^1 \times P^2$, the average value of V is zero. The potential U has the correct asymptotic behavior for both the near case, as we approach the degenerate $S^1 \times P^2$, and the far case as we approach asymptotic flatness at infinite distance. In the near case, the spacelike components of the metric have conformal weight ρ that scales like $1/r$ and preserves Ricci flatness on the $S^1 \times P^2$ in the same way as the 2-dimensional case. In the far case, the spacelike components of the metric have conformal weight ρ that scales like $e^{1/r}$ in the same way as a metric for any compact source with flat background. We therefore take as an approximation that $V = 0$ everywhere and that we can obtain this approximation from the Weyl metric by a coordinate transformation. (See [83] for some discussion of such a coordinate transformation.) We therefore arrive at the conformastatic metric

$$ds^2 = e^{-2\kappa}dt^2 - e^{2\kappa}(r^2d\phi^2 + dr^2 + dz^2) \quad (61)$$

such that κ is a harmonic function, where we note that κ is proportional to any harmonic function U whose source is the degenerate $S^1 \times P^2$.

In the previous section we had the problem that introducing the time dimension added a factor ρ to the volume element, and we dealt with that problem by adding motion to the embedding. Here we are introducing the ϕ dimension, and this adds another factor ρ to the volume element. The volume element of the manifold is dV/γ , and therefore if the manifold M is oriented such that $\gamma = \rho^2$, then a factor γ will compensate for the factors of ρ in both the t and ϕ coordinate. By comparison, in the 2+1 case, the conformal weight scales dt^2 by ρ^2 and the embedding introduces a factor $\gamma = \rho$, so that we have

$$\rho^2\left(\frac{dt}{\gamma}\right)^2 = \rho^2\left(\frac{1}{\rho^2}\right)dt^2 = dt^2. \quad (62)$$

In the 3+1 case, the dt^2 term scales by ρ^2 and the embedding introduces a factor $\gamma = \rho^2$, so that we have

$$\rho^2\left(\frac{1}{\rho^4}\right)dt^2 = \left(\frac{1}{\rho^2}\right)dt^2 = e^{-2\kappa}dt^2 \quad (63)$$

where we have used Equation (53). Again, the P^2 geometry can be expanded, and ρ compensates such that circumference is conserved. Likewise, as ρ reduces, $\gamma = \rho^2$ implies that the velocity of motion also reduces.

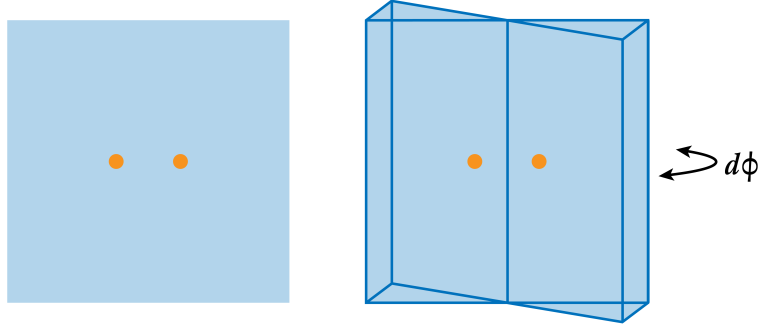


Figure A5: (a) We show \mathbb{R}^2 with degenerate P^2 at $(r, z, \phi) = (1, 0, 0)$ and $(r, z, \phi) = (1, 0, \pi)$. The harmonic function κ is $\kappa(x) = \sum_i -\ln(d(p_i, x))$. (b) We show a $d\phi$ slice from \mathbb{R}^3 with corresponding harmonic function κ that is weighted by $rd\phi$. The dots indicate the location of the degenerate $S^1 \times P^2$ in this $d\phi$ slice.

We call the distance from a point to the particle d . In three spatial dimensions, far away from a particle κ scales as $1/d$. Therefore $\lim_{d \rightarrow \infty} e^\kappa = \lim_{d \rightarrow \infty} e^{1/d} = 1$. This is in contrast to the 2-dimensional solution where κ scales like $-\ln(d)$, and ρ converges to zero at infinite distance. Therefore, in three dimensions it makes sense to say that at infinite distance $\rho = 1$ and $\gamma = \rho^2 = 1$.

Appendix D Obstruction to Single $\mathbb{R}^3 \# (S^1 \times P^2)$ Annihilation

In Section 6.5 we described how a pair of particles could annihilate while maintaining Ricci flatness. In Section 6.10 we described the P-contraction, and in so doing it may seem as if we introduced a way in which a single lepton could disappear while maintaining Ricci flatness.

The knot $\mathbb{R}^3 \# (S^1 \times P^2)$ can P-contract to $\mathbb{R}^3 \# (S^1 \times P^2)_*$. The P-contraction can still satisfy $\hat{R}^{\mu\nu} = 0$, meaning there is a ρ distribution such that the metric $g_{\mu\nu}$ is Ricci flat on $\mathbb{R}^3 \# (S^1 \times P^2)_*$. Suppose we could extend this P-contraction such that the $\mathbb{R}^3 \# (S^1 \times P^2)$ is P-contracted at every angle ϕ . This process would annihilate the $\mathbb{R}^3 \# (S^1 \times P^2)$ without needing to interact with another particle. What prevents this?

In the Appendix Section C, we described how $\mathbb{R}^3 \# (S^1 \times P^2)$ can satisfy the constraint $\hat{R}^{\mu\nu} = 0$. The solution requires motion such that the Lorentz factor γ is related to the conformal weight ρ by $\gamma = \rho^2$. Assume that the knot $\mathbb{R}^3 \# (S^1 \times P^2)_*$ is P-contracted over some non-zero length (more than just one point). Then the manifold has no extension into x^4 and x^5 along that length. Along the P-contracted segment, the rotational motion of the $\mathbb{R}^3 \# (S^1 \times P^2)_*$ is motion of the manifold parallel to itself, which is equivalent to no motion and $\gamma = 1$. Therefore the rotation of $\mathbb{R}^3 \# (S^1 \times P^2)_*$ does not compensate for ρ along the P-contracted segment in the way we worked out in the Appendix Section C. This implies that the manifold does not satisfy $\hat{R}^{\mu\nu} = 0$ there. This implies that it is not possible to P-contract a $\mathbb{R}^3 \# (S^1 \times P^2)_*$ on a segment of non-zero length. Therefore P-contraction cannot annihilate an individual $\mathbb{R}^3 \# (S^1 \times P^2)$.

Appendix E Quark Charge

We might wonder why we do not find in nature a quark without a charge. Is there a theoretical reason that a quark must have a charge? We address that question here. In a hadron the quarks are packed closely together, and the topology of the knots affects the curvature of the manifold. If the quarks are charged, the electromagnetic field changes the metric $g_{\mu\nu} = \rho^2 A_{\alpha,\mu} A^\alpha_{,\nu}$ and allows the constraint $\hat{R}^{\mu\nu} = 0$ to be maintained. Quarks have a complicated relationship between geometry and field, which explains how there can be multiple solutions for the charges of the quarks. Experimentally, there have been no indications of uncharged quarks, suggesting that the electric field is either necessary or maximizes

entropy in all observed cases.

Appendix F Obstruction to Charged and Unlinked P-contraction

In Section 6.10 we introduced the P-contraction, in which a knot may spontaneously change from one generation to another, for example, a muon neutrino to an electron neutrino or a strange to a down. We stipulated that the knot must be uncharged, and we outlined a mechanism by which a linked knot might become uncharged before its P-contraction. In this section we discuss why a charged, unlinked knot cannot P-contrast.

The electric field appears in the metric $g_{\mu\nu} = \rho^2 A_{\alpha,\mu} A_{\nu}^{\alpha}$ through derivatives of the A^{ν} field, namely through $A^0_{,\nu}$ and $A^{\nu}_{,0}$. On a charged knot $\mathbb{R}^3\#(S^1 \times P^2)$, the $A^0_{,\nu}$ derivatives come to a cusp on the knot. On the cusp, the second derivatives of A^{ν} are infinite. To preserve the constraint $\hat{R}^{\mu\nu} = 0$, there must be a geometric cusp with opposite curvature at the same location. At a P-contraction, the knot $\mathbb{R}^3\#(S^1 \times P^2)_*$ contracts the amplitude of the P^2 down to a point. If the knot were charged, then the cusp of the geometric curvature would have to also contract to a point. There is no way to contract that geometric curvature to a point, and therefore a charged $\mathbb{R}^3\#(S^1 \times P^2)$ cannot P-contrast by itself.

Appendix G Generation Limits

It is possible that further exploration of the theory will show that generations of neutrinos for $n > 2$ are disallowed. Here we present a possible explanation that neutrinos with $n > 2$ are not observed.

Let us assume neutrinos have mass of the order $0.1 \text{ eV}/c^2$. The mass cannot be less than the energy E from spin angular momentum L . We model the knot $\mathbb{R}^3\#(S^1 \times P^2)$ as a spinning ring of infinitesimal thickness. In the rest frame of the neutrino, the rotation of the ring is relativistic, and the integral of the magnitude of that momentum is approximately

$$p \approx \frac{E}{c} = 0.1 \text{ eV}/c. \quad (64)$$

If r is the length scale of the knot, then we have

$$pr \approx L \quad (65)$$

and

$$pr \approx \frac{\hbar}{2}. \quad (66)$$

From this we obtain $r \approx 1 \times 10^{-6} \text{ m}$, and the time-scale for light to traverse the neutrino in its own rest frame is $3 \times 10^{-15} \text{ s}$. According to one model [84] for the masses and mixing angles of the neutrinos, the tau neutrino and the muon neutrino oscillate over a distance given by

$$\frac{D}{E} \approx 500 \text{ km/GeV} \quad (67)$$

where E is the energy of the neutrino. If we use the rest energy of the neutrino 0.1 eV , then we can write the following for a time-scale in the rest frame of the neutrino: $\tau = \Delta t/\gamma$, where Δt is the time for an oscillation to occur in the lab frame

$$\begin{aligned} \tau &= \frac{\Delta t}{\gamma} = \frac{D}{c\gamma} = \frac{\gamma m D}{Ec\gamma} = \frac{Dm}{Ec} \\ \tau &= \left(\frac{5 \times 10^5 \text{ m}}{10^9 \text{ eV}} \right) \left(\frac{0.1 \text{ eV}}{3 \times 10^8 \text{ m/s}} \right) \approx 2 \times 10^{-13} \text{ s}. \end{aligned} \quad (68)$$

In the rest frame of the neutrino, the oscillation happens on a time scale that is comparable to the time for light to traverse the neutrino. For oscillations between generations $n = 2$ and higher the transition may occur too fast for the particle to establish a mass eigenstate. We therefore expect three distinguishable generations of neutrino masses corresponding to $\mathbb{R}^3\#(S^1 \times P^2)_0$, $\mathbb{R}^3\#(S^1 \times P^2)_1$, and $\mathbb{R}^3\#(S^1 \times P^2)_n$ for $n \geq 2$.

Further exploration of the theory may show that generations of charged fermions with $n > 2$ are not seen because of energy and stability or are disallowed for other reasons.

Appendix H Particle Size

Charged leptons have always appeared pointlike in collision experiments, but the assumption of pointlike charged particles has presented a number of theoretical problems. In this theory a fermion is represented by a knot, and a knot has a finite size. We saw how to find an estimate of the size of a knot in Section G. We can calculate a lower bound for the size of a charged fermion far from other particles. Consider, for example, an electron, which has mass $0.5 \text{ MeV}/c^2$. In the neutrino calculation we assumed the rest energy was almost all due to angular momentum, while in the case of the electron, the rest energy is an upper bound for angular momentum energy. In this case we obtain $r \gtrsim 2 \times 10^{-13} \text{ m}$.

In this theory the geometry of a knot, and thus its size, depends on its proximity to other knots. We showed in Section C that the conformal weight ρ can be described in terms of a harmonic function κ such that $\rho = e^\kappa$. The harmonic function κ increases as it approaches the knot $\mathbb{R}^3 \# (S^1 \times P^2)$. If there are multiple knots $\mathbb{R}^3 \# (S^1 \times P^2)$, then each contributes its own harmonic function κ_i , and the conformal weight is $\rho = \exp(\sum_i \kappa_i)$. As a charged knot is approached by another charged knot, the value of ρ near that knot increases. To conserve charge, the diameter of the knot reduces as the distance to other knots reduces. As distance goes to zero, the size of the charged lepton knot goes to zero. Therefore the electron appears to be pointlike in collisions.

Quarks, by contrast, are linked to other knots and are constantly in close proximity. The constraint $\tilde{R}^{\mu\nu} = 0$ requires that the quarks are in relative motion so that the Lorentz factor γ can counter the effect of proximity on the conformal weight ρ . Interaction of quarks with other particles has a smaller effect on their apparent size.

H.1 Recombination of Branches is Equivalent to Addition of Quantum Amplitudes ψ

If multiple collections of branches with knots recombine, the quantum amplitude of the union of the recombining collections is equal to the sum of the quantum amplitudes of the individual collections. To show this, we use multiple indices such that we have multiple collections of branches C_m , each of which consists of branches B_{mn} that have knot amplitudes a_{mn} and weight coefficients k_{mn} .

In each of the collections C_m individually, there are total weight coefficients k_m , weighted average amplitudes \bar{a}_m , and quantum amplitudes ψ_m as follows:

$$k_m = \sum_n k_{mn} \quad (69)$$

$$\bar{a}_m = \left(\sum_n k_{mn} \right)^{-1} \left(\sum_n k_{mn} a_{mn} \right) \quad (70)$$

$$\psi_m = \left(\sum_n k_{mn} a_{mn} \right) = k_m \bar{a}_m. \quad (71)$$

See eqns. (25), (26), (27), and (28) in the text. If all the branches in all of the collections C_m recombine, then they have a total weight coefficient k , weighted average amplitude \bar{a} , and quantum amplitude ψ as follows:

$$k = \sum_m \sum_n k_{mn} = \sum_m k_m \quad (72)$$

$$\bar{a} = \left(\sum_m \sum_n k_{mn} \right)^{-1} \left(\sum_m \sum_n k_{mn} a_{mn} \right) = \left(\sum_m k_m \right)^{-1} \left(\sum_m k_m \bar{a}_m \right) \quad (73)$$

$$\psi = \left(\sum_m \sum_n k_{mn} a_{mn} \right) = \left(\sum_m \sum_n k_{mn} \right) \bar{a} = \left(\sum_m k_m \right) \left(\sum_m k_m \right)^{-1} \left(\sum_m k_m \bar{a}_m \right) = \left(\sum_m k_m \bar{a}_m \right) = \sum_m \psi_m. \quad (74)$$

Therefore the quantum amplitude of the union of all the branches in all the collections C_m is the sum of the quantum amplitudes, $\psi = \sum_m \psi_m$. Likewise, the quantum amplitude of the union has the same relationship to the weighted average of the union, $\psi = \left(\sum_m k_m \bar{a}_m \right) = k \bar{a}$.

Appendix I The Lagrangian is Optimized by a Single Rotation Direction in the Co-dimension

Particle dynamics and gravitational dynamics both result in rotation of the manifold of the form $(x^0, x^1, x^2, x^3) \mapsto (x^0, x^1, x^2, x^3, b \sin(k_j x^j), b \cos(k_j x^j))$ where $j = 0, 1, 2, 3$, and b is the amplitude. The Lagrangian is maximized when the average velocity of rotation is maximized. We show here that the average velocity of rotation is maximized when the direction of rotation is the same for every contributing source, that is, when the sign of k_0 is the same for all sources.

If we introduce a single rotational source, then we can say its motion is of the form $(t, x^1, x^2, x^3, f^4, f^5)$ in f^4 and f^5 . We can express the motion using a complex number such that $f^4 + f^5 i = r_1 e^{i\omega_1 t}$. The linearized Ricci flatness constraint is approximately a wave equation, and the motion from the rotational source propagates outward like a wave. That motion can have one of two directions with either $\omega_1 > 0$ or $\omega_1 < 0$. The velocity is therefore

$$v = \frac{d}{dt} (r_1 e^{i\omega_1 t}) = i\omega_1 r_1 e^{i\omega_1 t}. \quad (75)$$

Even for a single source, there is some variation in the magnitude r_1 and the angular velocity ω_1 . We construct a probability distribution to model the displacement $r_1 e^{i\omega_1 t}$. We also construct a probability distribution to model the velocity $i\omega_1 r_1 e^{i\omega_1 t}$ associated with each displacement. Figure A6(a) shows a piece of the manifold with a source of rotational motion shown by the black point and the magnitude of the motion that it induces shown in green. We take a sample of that motion at the blue point. Sampling that motion at the blue point over time generates a probability distribution $P(x^4, x^5)$ for the probability of finding the point with those x^4 and x^5 coordinates. That distribution is shown in Figure A6(b). The motion of the point is correlated to its position, and for every value of (x^4, x^5) there is a probability distribution of velocities $V(x^4, x^5)$. Figure A6(c) shows the expected value of $V(x^4, x^5)$ at each value of x^4 and x^5 .

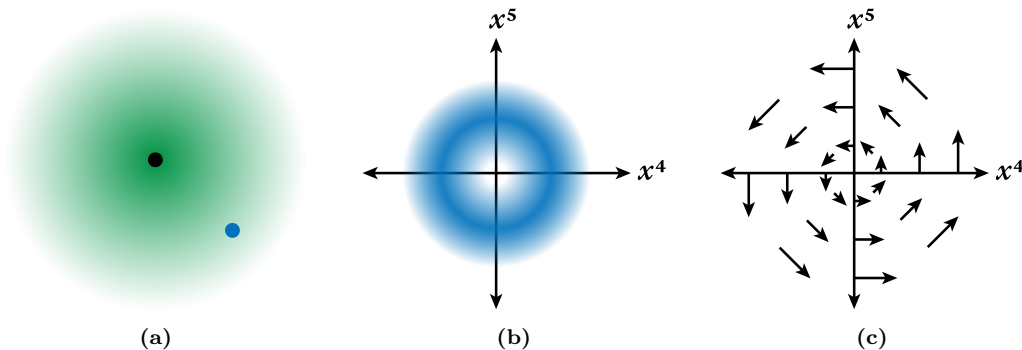


Figure A6: (a) There is a single source for rotational motion on the manifold, the black point. The magnitude of the rotational motion is shown in green. We take a sample of that motion at the point shown in blue. (b) We show the probability distribution for displacement at that point. The distribution corresponds to $r_1 e^{i\omega_1 t}$ with variation of r_1 and ω_1 . (c) We show the expected value of the velocity of rotation corresponding to each value of the displacement. The distribution corresponds to $i\omega_1 r_1 e^{i\omega_1 t}$ with variation of r_1 and ω_1 .

We now create the displacement and velocity probability distributions that result from multiple sources. For both displacement and velocity, the distribution of the sum is the convolution of the individual distributions. Now if we assume that we can choose the direction of rotation of each of the sources, then we maximize the Lagrangian by maximizing the magnitude of the velocities in the combined velocity distribution. This results from having all the contributing rotational sources rotating in the same direction.

References

1. Parker, L. & Toms, D. *Quantum field theory in curved spacetime: quantized fields and gravity* (Cambridge university press, 2009).
2. Deser, S. & Levin, O. Accelerated detectors and temperature in (anti-) de Sitter spaces. *Classical and Quantum Gravity* **14**, L163 (1997).
3. Deser, S. & Levin, O. Equivalence of Hawking and Unruh temperatures and entropies through flat space embeddings. *Classical and Quantum Gravity* **15**, L85 (1998).
4. Deser, S. & Levin, O. Mapping Hawking into Unruh thermal properties. *Physical Review D* **59**, 064004 (1999).
5. Finkelstein, R. J. The elementary particles as quantum knots in electroweak theory. *International Journal of Modern Physics A* **22**, 4467–4480 (2007).
6. Finkelstein, R. J. Knots and preons. *International Journal of Modern Physics A* **24**, 2307–2316 (2009).
7. Faddeev, L. & Niemi, A. J. Knots and particles. *arXiv preprint hep-th/9610193* (1996).
8. Williams, R. F. Expanding attractors. *Publications Mathématiques de l'Institut des Hautes Études Scientifiques* **43**, 169–203 (1974).
9. Kibble, T. W. The standard model of particle physics. *European Review* **23**, 36–44 (2015).
10. CERN. *The standard model* <http://home.web.cern.ch/about/physics/standard-model>. Accessed: 08.02.2021.
11. Will, C. Was Einstein Right? Testing Relativity at the Centenary. In 100 Years of Relativity: Space-time Structure: Einstein and Beyond, edited by A. Ashtekar. *arXiv preprint gr-qc/0504086* (2005).
12. 't Hooft, G. & Veltman, M. Regularization and renormalization of gauge fields. *Nuclear Physics B* **44**, 189–213 (1972).
13. Polchinski, J. *String theory: Volume 2, superstring theory and beyond* (Cambridge university press, 1998).
14. Susskind, L. The anthropic landscape of string theory. *arXiv preprint hep-th/0302219* (2003).
15. Rovelli, C. *Quantum gravity* (Cambridge university press, 2004).
16. Zeeman, E. C. Unknotting combinatorial balls. *Annals of Mathematics*, 501–526 (1963).
17. Elsheikh, M. N. Schrödinger Operators on Graphs and Branched Manifolds. *Journal of Applied Mathematics and Physics* **2014** (2014).
18. Ehlers, J., Pirani, F. A. & Schild, A. Republication of: The geometry of free fall and light propagation. *General Relativity and Gravitation* **44**, 1587–1609 (2012).
19. Fischer, A. E., Wolf, J. A., *et al.* The structure of compact Ricci-flat Riemannian manifolds. *Journal of Differential Geometry* **10**, 277–288 (1975).
20. Bajkova, A. T. The generalization of maximum entropy method for reconstruction of complex functions. *Astronomical and Astrophysical Transactions* **1**, 313–320 (1992).
21. Ranicki, A. *High-dimensional knot theory: Algebraic surgery in codimension 2* (Springer Science & Business Media, 2013).
22. Feynman, R. P., Hibbs, A. R. & Styer, D. F. *Quantum mechanics and path integrals* (Courier Corporation, 2010).
23. Friedberg, R. & Lee, T. Discrete quantum mechanics. *Nuclear Physics B* **225**, 1–52 (1983).
24. Johnson, J. K. *Convex relaxation methods for graphical models: Lagrangian and maximum entropy approaches* PhD thesis (Massachusetts Institute of Technology, Department of Electrical Engineering ..., 2008).
25. Zwiebach, B. *A first course in string theory* 2nd ed. (Cambridge university press, 2009).
26. Ekholm, T., Etnyre, J. & Sullivan, M. The contact homology of Legendrian submanifolds in R^{2n+1} . *Journal of Differential Geometry* **71**, 177–305 (2005).

27. Avrin, J. A visualizable representation of the elementary particles. *Journal of Knot Theory and Its Ramifications* **14**, 131–176 (2005).
28. Avrin, J. Flattened Moebius strips: Their physics, geometry and taxonomy. *Journal of Knot Theory and Its Ramifications* **17**, 835–876 (2008).
29. Avrin, J. On the taxonomy of flattened Moebius strips. *Journal of Knot Theory and Its Ramifications* **21**, 1250004 (2012).
30. Avrin, J. Torus knots embodying curvature and torsion in an otherwise featureless continuum. *Journal of Knot Theory and Its Ramifications* **20**, 1723–1739 (2011).
31. Bandyopadhyay, P. *Geometry, topology and quantization* (Springer Science & Business Media, 2013).
32. Morse, P. M. & Feshbach, H. Methods of theoretical physics. *American Journal of Physics* **22**, 410–413 (1954).
33. Korn, G. A. & Korn, T. M. *Mathematical handbook for scientists and engineers: definitions, theorems, and formulas for reference and review* (Courier Corporation, 2000).
34. Margenau, H., Murphy, G. M., *et al.* *Mathematics of physics and chemistry* (1956).
35. Moon, P. & Spencer, D. E. *Field theory handbook: including coordinate systems, differential equations and their solutions* (Springer, 2012).
36. Cowan, T. M. *et al.* *Knots and applications* (World Scientific, 1995).
37. Geroch, R. P. Topology in general relativity. *Journal of Mathematical Physics* **8**, 782–786 (1967).
38. Kohno, T. *New developments in the theory of knots* (World scientific, 1990).
39. Avrin, J. S. Knots on a Torus: A model of the Elementary particles. *Symmetry* **4**, 39–115 (2012).
40. Buniy, R. V. & Kephart, T. W. A model of glueballs. *Physics Letters B* **576**, 127–134 (2003).
41. Ng, S. K. On a knot model of mesons and baryons. *arXiv preprint hep-th/0210024* (2002).
42. Avrin, J. S. *Knots, Braids And Mobius Strips-Particle Physics And The Geometry Of Elementarity: An Alternative View* (World scientific, 2015).
43. Finkelstein, R. J. A knot model suggested by the standard electroweak theory. *International Journal of Modern Physics A* **20**, 6487–6494 (2005).
44. Christandl, M. *et al.* Perfect transfer of arbitrary states in quantum spin networks. *Physical Review A* **71**, 032312 (2005).
45. Hein, M. *et al.* Entanglement in graph states and its applications. *arXiv preprint quant-ph/0602096* (2006).
46. Ionicioiu, R. & Spiller, T. P. Encoding graphs into quantum states: an axiomatic approach. *Physical Review A* **85**, 062313 (2012).
47. Kleinert, H. *Path integrals in quantum mechanics, statistics, polymer physics, and financial markets* (World scientific, 2009).
48. MacKenzie, R. Path integral methods and applications. *arXiv preprint quant-ph/0004090* (2000).
49. Witten, E. Fivebranes and knots. *Quantum Topology* **3**, 1–137 (2012).
50. Simonyi, G. Graph entropy: a survey. *Combinatorial Optimization* **20**, 399–441 (1995).
51. Simonyi, G. Perfect graphs and graph entropy. An updated survey. *Perfect graphs*, 293–328 (2001).
52. Bialas, P. & Oleś, A. K. Correlations in connected random graphs. *Physical Review E* **77**, 036124 (2008).
53. Kreimer, D. *Knots and Feynman diagrams* **13** (Cambridge University Press, 2000).
54. Luse, K. M. *Invariants of knots, graphs, and Feynman diagrams* (The George Washington University, 2008).
55. Pettini, M. *Geometry and topology in Hamiltonian dynamics and statistical mechanics* (Springer Science & Business Media, 2007).
56. Landau, L. & Lifshitz, E. *Classical Theory of Fields, Fourth Revised English Edition* (Pergammon Press, 1975).
57. Slavov, B. *et al.* The Photon as a Soliton: I. Planck’s Density of Radiation. *Comptes Rendus de l’Academie Bulgare des Sciences* **53**, 6–43 (2000).

58. Kamenov, P. & Slavov, B. The photon as a soliton. *Foundations of Physics Letters* **11**, 325–342 (1998).
59. Weinberg, S. A model of leptons. *Physical review letters* **19**, 1264 (1967).
60. Salam, A. & Ward, J. Electromagnetic and weak interactions. *Physics Letters* **13**, 168–171. ISSN: 0031-9163 (1964).
61. Glashow, S. L., Iliopoulos, J. & Maiani, L. Weak interactions with lepton-hadron symmetry. *Physical review D* **2**, 1285 (1970).
62. Gell-Mann, M. *The eightfold way* (CRC Press, 2018).
63. Okubo, S. Note on unitary symmetry in strong interactions. *Progress of Theoretical Physics* **27**, 949–966 (1962).
64. Sakurai, J. J. *Currents and mesons* (University of Chicago press, 1969).
65. Rosenzweig, C., Schechter, J. & Trahern, C. Is the effective Lagrangian for quantum chromodynamics a σ model? *Physical Review D* **21**, 3388 (1980).
66. Di Vecchia, P. & Veneziano, G. Chiral dynamics in the large N limit. *Nuclear Physics B* **171**, 253–272 (1980).
67. Witten, E. Large N chiral dynamics. *Annals of Physics* **128**, 363–375 (1980).
68. Lucha, W., Schöberl, F. F. & Gromes, D. Bound states of quarks. *Physics reports* **200**, 127–240 (1991).
69. Weinberg, S. The U (1) problem. *Physical Review D* **11**, 3583 (1975).
70. Dmitrašinović, V. U A (1) breaking and scalar mesons in the Nambu and Jona-Lasinio model. *Physical Review C* **53**, 1383 (1996).
71. Dmitrašinović, V. Effective quark operator models of U A (1) symmetry breaking. *Physical Review D* **56**, 247 (1997).
72. Blask, W., Bohn, U., Huber, M., Metsch, B. C. & Petry, H. Hadron spectroscopy with instanton induced quark forces. *Zeitschrift für Physik A Atomic Nuclei* **337**, 327–335 (1990).
73. Klempt, E., Metsch, B., Münz, C. & Petry, H. Scalar mesons in a relativistic quark model with instanton-induced forces. *Physics Letters B* **361**, 160–166 (1995).
74. Ritter, C., Metsch, B. C., Münz, C. & Petry, H. Instanton effects in the decay of scalar mesons. *Physics Letters B* **380**, 431–436 (1996).
75. Burakovsky, L., Goldman, T. & Horwitz, L. New quadratic baryon mass relations. *Physical Review D* **56**, 7124 (1997).
76. Burakovsky, L. & Goldman, T. Gell-Mann-Okubo mass formula revisited. *arXiv preprint hep-ph/9708498* (1997).
77. Gambini, R. & Pullin, J. Knot theory and the dynamics of quantum general relativity. *Classical and Quantum Gravity* **13**, L125 (1996).
78. Kauffman, L. H. *et al. Series on Knots and Everything* (World Scientific Press: Singapore, 2011).
79. York Jr, J. W. Role of conformal three-geometry in the dynamics of gravitation. *Physical review letters* **28**, 1082 (1972).
80. Gibbons, G. W. The Einstein action of Riemannian metrics and its relation to quantum gravity and thermodynamics. *Physics Letters A* **61**, 3–5 (1977).
81. Hawking, S. W. & Horowitz, G. T. The gravitational Hamiltonian, action, entropy and surface terms. *Classical and Quantum Gravity* **13**, 1487 (1996).
82. Besse, A. L. *Einstein manifolds* (Springer Science & Business Media, 2007).
83. D’Afonseca, L., Letelier, P. & Oliveira, S. Geodesics around Weyl–Bach’s ring solution. *Classical and Quantum Gravity* **22**, 3803 (2005).
84. Beringer, J. *et al. PDG Live Particle Summary Quarks (u, d, s, c, b, t, b’, t’, Free)*. *Particle Data Group, PR D86, 010001* 2012.